



Deposited via The University of Leeds.

White Rose Research Online URL for this paper:

<https://eprints.whiterose.ac.uk/id/eprint/166332/>

Version: Accepted Version

Article:

Moore, J, Beinlich, A, Piazzolo, S et al. (2020) Metamorphic Differentiation via Enhanced Dissolution along High Permeability Zones. *Journal of Petrology*, 61 (10). egaa096. ISSN: 0022-3530

<https://doi.org/10.1093/petrology/egaa096>

Reuse

Items deposited in White Rose Research Online are protected by copyright, with all rights reserved unless indicated otherwise. They may be downloaded and/or printed for private study, or other acts as permitted by national copyright laws. The publisher or other rights holders may allow further reproduction and re-use of the full text version. This is indicated by the licence information on the White Rose Research Online record for the item.

Takedown

If you consider content in White Rose Research Online to be in breach of UK law, please notify us by emailing eprints@whiterose.ac.uk including the URL of the record and the reason for the withdrawal request.

Draft Manuscript for Review

Metamorphic Differentiation via Enhanced Dissolution along High Permeability Zones

Journal:	<i>Journal of Petrology</i>
Manuscript ID	JPET-Jun-20-0083.R1
Manuscript Type:	Original Manuscript
Date Submitted by the Author:	13-Sep-2020
Complete List of Authors:	Moore, Jo; The Institute for Geoscience Research, Curtin University, School of Earth and Planetary Sciences Beinlich, Andreas; The Institute for Geoscience Research, Curtin University, School of Earth and Planetary Sciences; University of Bergen, Department of Earth Science Piazolo, Sandra ; University of Leeds, Austrheim, Håkon; Physics of Geological Processes, University of Oslo Putnis, Andrew; Curtin University, The Institute for Geoscience Research; University of Münster, Institut für Mineralogie
Keyword:	Amphibolite facies, dissolution precipitation, mass transfer, metamorphic differentiation, thermodynamic modelling

SCHOLARONE™
Manuscripts

1 **Metamorphic Differentiation via Enhanced** 2 **Dissolution along High Permeability Zones**

3 **Jo Moore^{1*}, Andreas Beinlich^{1,2}, Sandra Piazzolo³, Håkon Austrheim⁴, Andrew Putnis^{1,5}**

4 *¹The Institute for Geoscience Research (TIGeR), School of Earth and Planetary Sciences, Curtin*
5 *University, Perth, WA, 6845, Australia*

6 *²Department of Earth Science, University of Bergen, Allégaten 41, 5007 Bergen, Norway*

7 *³School of Earth and Environment, University of Leeds, Leeds, UK*

8 *⁴Physics of Geological Processes (PGP), The Njord Centre, Department of Geosciences,*
9 *University of Oslo, 0316, Oslo, Norway*

10 *⁵Institut für Mineralogie, University of Münster, 48149 Münster, Germany*

11 ** Corresponding author (Tel: +61403560643 E-mail: josephine.moore@postgrad.curtin.edu.au)*

12 **ABSTRACT**

13 Metamorphic differentiation, resulting in segregated mineral bands, is commonly recorded in
14 metamorphic rocks. Despite the ubiquitous nature of compositionally layered metamorphic
15 rocks, the processes that are responsible for metamorphic differentiation receive very little
16 attention. Here, detailed petrography, quantitative mineral chemistry and bulk rock analyses are
17 applied to investigate compositional variations and assemblage microstructure. Furthermore,
18 thermodynamic modelling is applied to provide additional constraints on the P–T–X_{H₂O}
19 conditions of assemblage formation and mass transfer. The studied outcrop, located within the
20 Bergen arcs of southwestern Norway, preserves the hydration of anorthositic granulite at
21 amphibolite-facies conditions. The amphibolite-facies hydration is expressed as both a statically
22 hydrated amphibolite and a shear zone lithology, defined by the interlayering of amphibolite with

1
2
3 23 leucocratic domains. Within the granulite, quartz-lined fractures surrounded by amphibolite-
4
5 24 facies alteration haloes represent relics of initial fluid infiltration associated with brittle failure.
6
7
8 25 The fracture assemblage (quartz + plagioclase + zoisite + kyanite ± muscovite ± biotite) is
9
10 26 identical to that occurring within leucocratic domains of the shear zone. Consequently, the
11
12 27 compositional layering of the shear zone lithology is linked to fluid infiltration along localised
13
14 28 zones of high permeability that result from fracturing. Mass-balance calculations indicate that
15
16 29 quartz-lined fractures and compositional differentiation of the shear zone resulted from mass
17
18 30 redistribution internal to the shear zone rather than partial melting or precipitation of minerals
19
20 31 from externally derived fluid. The process of internal fractionation within the shear zone is
21
22 32 driven by enhanced dissolution along highly permeable fracture planes resulting in the loss of
23
24 33 MgO, Fe^{tot} and K₂O from the leucocratic domains. Elements dissolved in the fluid are then
25
26 34 transported and ultimately either precipitated in comparatively impermeable amphibolite
27
28 35 domains or removed from the system resulting in an overall mass loss. The mass transfer causing
29
30 36 metamorphic differentiation of the shear zone is the result of coupled reaction and diffusion
31
32 37 under differential stress. The mechanisms of mass redistribution observed within this shear zone
33
34 38 provides further insight into the processes that facilitate mass transfer in the Earth's crust.

39 **Key words**

40 Amphibolite facies; dissolution precipitation; mass transfer; metamorphic differentiation;
41 thermodynamic modelling

42 INTRODUCTION

43 Fluid-driven mass transfer is a vital component of the processes that facilitate the chemical
44 differentiation of the Earth's crust, the formation of mineral deposits and local lithospheric
45 weakening. Mass transfer may be recorded at many scales in metamorphic rocks. At large scales,
46 mass transfer may be responsible for volume losses during regional metamorphism (see e.g.
47 Ague, 1994) and ductile shearing (see e.g. Dipple & Ferry, 1992, Selverstone *et al.*, 1991) as
48 well as volume increase in extensional settings, generally expressed by the formation of veins or
49 dykes. At the mm-cm scale, mass transfer is expressed by formation of local mineral
50 assemblages and compositional banding, and at the grain-scale it may be observed as
51 compositional zoning in minerals (Putnis & Austrheim, 2013). Understanding the processes
52 responsible for compositional banding in metamorphic rocks, often referred to as metamorphic
53 differentiation (Williams, 1972, 1990), is important as the processes driving and facilitating
54 diffusional mass transfer are likely independent of the scale of the system. A better
55 understanding of the driving forces behind metamorphic differentiation should therefore provide
56 better insight to mass transfer processes in the crust as a whole.

57 The processes that facilitate metamorphic differentiation have been discussed extensively
58 in the framework of experimental studies and observations of metasedimentary sequences
59 (Dipple *et al.*, 1990, Fisher, 1970, Vernon, 1979, Vernon, 1998, Williams, 1990, Wintsch *et al.*,
60 1991, Wintsch & Andrews, 1988). While a general consensus on the exact mechanisms behind
61 metamorphic differentiation has not been met, two broad requirements are consistent amongst
62 most contributions; an imposing differential stress (Dewers & Ortoleva, 1990) and transport
63 along a chemical potential gradient (Bons & Jessell, 1997, Dipple *et al.*, 1990, Fisher, 1970,
64 Joesten, 1977). In most metamorphic environments, reactions occurring due to mm-cm scale

1
2
3 65 chemical potential gradients will be reliant on the presence of a grain boundary fluid phase
4
5 66 (Fisher, 1970, Rutter, 1983). Experimental evidence indicates that the rate of intergranular solid-
6
7
8 67 state diffusion is sluggish in comparison to diffusion through an intergranular fluid medium
9
10 68 (Carlson, 2010, Rubie, 1986, Yund, 1997). By comparison, the intergranular diffusion of
11
12 69 elements through grain boundary fluid – commonly referred to as either pressure solution or
13
14 70 dissolution-precipitation creep – occurs at significantly faster rates (Oelkers & Helgeson, 1988)
15
16 71 potentially inducing large-scale rock transformations on short timescales (Beinlich *et al.*, 2020).
17
18 72 Hence, diffusion through interconnected grain boundary fluid will enable significant mass
19
20 73 transport through the crust wherever the rock is sufficiently saturated with fluid and may link
21
22 74 areas of incompatible equilibrium conditions, i.e. drive mass transport along a chemical potential
23
24 75 gradient.
25
26
27
28

29 76 Earlier studies on metamorphic differentiation via mass transfer were focused on the
30
31 77 exchange of elements between adjacent sedimentary layers, and thus the chemical potential
32
33 78 gradient could be attributed to the incompatibility of the original compositional layering during
34
35 79 metamorphism (e.g. Orville, 1969, Vidale, 1969, Williams, 1972). In the cases where mass
36
37 80 transfer has effected a relatively homogenous protolith and/or mass transfer is occurring on a
38
39 81 scale larger than that defined by compositional layering, the driving force responsible for
40
41 82 creating the chemical potential gradient is inferred to be either directly or indirectly the result of
42
43 83 the imposed differential stress during metamorphism. In studies where the chemical potential
44
45 84 gradient is inferred to be a direct result of differential stress, local equilibrium conditions may be
46
47 85 created by the translation of the heterogeneous stress field to local thermodynamic pressures
48
49 86 (Dahlen, 1992, Wheeler, 2014, 2018). Consequently, high pressure metamorphic assemblages
50
51 87 would form where the normal stress is at a maximum. Indirectly, differential stress has been
52
53
54
55
56
57
58
59
60

1
2
3 88 theorised to induce chemical potential gradients by affecting reaction kinetics. For example,
4
5 89 dissolution is inferred to be enhanced at high stress boundaries while precipitation will be
6
7 90 enhanced at low stress sites due to the creation of cavities (Rutter, 1976). The local reaction that
8
9 91 occurs will be dependent on the rate-controlling step, whether that be dissolution, precipitation or
10
11 92 mass transport, the rate-controlling step should differ depending on the local conditions. If,
12
13 93 within the same rock, local zones of opposing reaction kinetics are connected by a grain
14
15 94 boundary fluid then this is likely to result in a local chemical potential gradient. This has been
16
17 95 demonstrated to occur during diagenesis, during which heterogeneous permeability distributions
18
19 96 under conditions favourable for dissolution-precipitation-driven reaction result in the formation
20
21 97 of a compositionally banded rock (Kelka *et al.*, 2017). While earlier work has primarily
22
23 98 addressed the processes driving the mass transfer and the resulting metamorphic differentiation
24
25 99 and volume loss in metasedimentary rocks, the same fundamental processes should be applicable
26
27 100 to all metamorphic rocks.
28
29
30
31
32

33 101 Here we present a detailed analysis of the amphibolite-facies hydration of relatively
34
35 102 homogenous anorthositic granulite of the Bergen arcs, southwestern Norway. In the outcrop,
36
37 103 texturally uniform statically hydrated amphibolite-facies rocks sharply transition into a
38
39 104 compositionally layered rock in a shear zone, providing an ideal locality to investigate the
40
41 105 processes behind fluid and strain-facilitated mass transfer and metamorphic differentiation.
42
43 106 Comparison of textural observations and chemical distribution amongst these lithologies suggest
44
45 107 that dissolution is enhanced in zones of relatively high permeability, producing chemical
46
47 108 potential gradients that then drive mass transfer.
48
49
50
51
52
53
54
55
56
57
58
59
60

109 GENERAL GEOLOGICAL BACKGROUND

110 The Bergen arcs constitute the hanging wall of the extensional Bergen arc shear zone. It is
111 defined as a set of nappes, including the focus of this study, the Lindås Nappe (Fig. 1a). The
112 Lindås Nappe mainly consists of an anorthosite-mangerite-charnockite-granite (AMCG) suite
113 and banded gneiss complexes. Following intrusion pulses between $1237 \pm 45/-35$ Ma to 945 ± 33
114 Ma (Austrheim, 1990, Bingen *et al.*, 2001), the magmatic suite has undergone pervasive
115 recrystallization at granulite facies conditions. The timing of the granulite facies recrystallization
116 is constrained between 929 Ma (Bingen *et al.*, 2001) and 910 ± 10 Ma (Cohen *et al.*, 1988).
117 Subsequently, Caledonian (~460-400 Ma) metamorphism along fluid conduits resulted in the
118 localized transformation of the Lindås Nappe granulite to either amphibolite or eclogite, the
119 latter of which is restricted to the westernmost extension of the nappe on the island of Holsnøy
120 (Austrheim, 1987, Bingen *et al.*, 2001, Boundy *et al.*, 1996, Glodny *et al.*, 2002, 2008, Moore *et*
121 *al.*, 2020).

122 The study outcrop is located on Radøy and preserves a Caledonian granulite to
123 amphibolite reaction interface. Here, amphibolite-facies alteration has been constrained to
124 ambient conditions of ~590-730°C and 10-14 kbar, based on thermodynamic modelling of the
125 hydration of the granulite along grain boundaries (Moore *et al.*, 2019), Zr-in-rutile thermometry,
126 and Al-in-hornblende barometry (Moore *et al.*, 2020). These P–T estimates are consistent with
127 previous estimates of 690°C and 10–12 kbar (Boundy *et al.*, 1996), obtained using cation
128 exchange thermobarometry in petrographically similar amphibolites of the Bergen arcs.

129 At the hydration interface, the amphibolite-facies assemblage inherits the overall texture
130 of the granulite (Fig. 1c). As the amphibolite-facies rock becomes highly strained within the

1
2
3 131 shear zone, it grades into compositionally distinct light and dark bands (Fig. 1b and e), allowing
4
5 132 for a detailed investigation of the interplay between strain, inferred stress and mass transfer.
6
7

8 9 133 **DESCRIPTION OF OUTCROP LITHOLOGIES**

10
11 134 Three main rock types are present in the outcrop at Fjellsende; granulite, amphibolite, and the
12
13 135 shear zone lithology consisting of a spaced foliation defined by bands of amphibolite and
14
15 136 leucocratic feldspar-rich domains (Fig. 1b-e). The granulite away from the shear zone is
16
17 137 characterised as a foliated, lilac coloured, and corona-bearing medium grained rock. In the
18
19 138 granulite, the foliation is defined by the alignment of 1- 2 cm elongate, mafic clusters, consisting
20
21 139 of diopside with garnet rims (Fig. 1c and d). At the granulite-amphibolite interface, hydration
22
23 140 occurs via static replacement, evidenced by the continuity of the granulite foliation into the
24
25 141 amphibolite (Fig. 1c). The amphibolite foliation, defined by elongate 1-2 cm clusters of
26
27 142 amphibole, bends sharply within 50 cm of the shear zone boundary (Fig. 1b), thus forming a
28
29 143 “strained” amphibolite. The foliation in the strained amphibolite is characterised by spaced 1-3
30
31 144 mm wide discontinuous amphibole-rich lenses surrounded by feldspar-rich domains. Within the
32
33 145 strained amphibolite, foliation-parallel 1 cm wide bands of creamy pinkish feldspar and quartz
34
35 146 appear at ~10 cm intervals. The shear zone lithology is characterized by the interlayering of dark
36
37 147 and leucocratic bands (Fig. 1e). Dark bands are defined by a mixture of amphibole and feldspar,
38
39 148 consistent with the mineralogy of the amphibolite. The leucocratic domains, which appear as
40
41 149 creamy white bands, are mainly composed of feldspar with strongly aligned clinozoisite.
42
43
44
45
46
47
48

49 150 In addition to the three main rock types, veins and fractures are also observed. Pinkish 1 -
50
51 151 2 cm thick veins in the granulite are composed of scapolite and continue as brown-black
52
53 152 discontinuous lenses, consisting of scapolite and amphibole, across the hydration interface into
54
55 153 the amphibolite. Fractures are only clearly observed within the granulite and occur as sub-
56
57
58
59
60

1
2
3 154 parallel stringers, striking approximately NW-SE (Fig. 1d). Haloes around quartz-lined fractures
4
5 155 are composed of milky feldspar and coronas that have been partially replaced by amphibole.
6
7

8 9 156 **METHODS**

10 11 157 **Sample preparation**

12
13
14 158 For the granulite, amphibolite and the shear zone lithologies, thin section blocks and epoxy
15
16 159 mounts were prepared parallel to the lineation (X direction) and normal to the foliation (XZ
17
18 160 plane). Sections were carbon coated for scanning electron microscopy (SEM) and mineral
19
20 161 chemical analysis.
21
22

23 24 162 **Petrography and imaging**

25
26
27 163 Microstructure was characterised with a standard petrographic microscope using plane-polarized
28
29 164 light (PPL) and cross-polarized light (XPL). Backscattered electron (BSE) imaging was
30
31 165 performed on the TESCAN MIRA variable pressure field emission scanning electron microscope
32
33 166 (FE-SEM) at the John de Laeter Centre (JdLC), Curtin University, Perth, Australia. Imaging was
34
35 167 performed with a beam energy of 25 kV at a working distance of 15 mm.
36
37

38 39 168 **Quantification of phase abundance**

40
41 169 Eight polished thin sections and 3 epoxy mounts were analysed using the TESCAN Integrated
42
43 170 Mineral Analyser (TIMA3) FE-SEM at the JdLC, Curtin University, Perth, Australia. Analyses
44
45 171 were performed using 4 PulseTor 30 energy dispersive X-ray (EDX) detectors at a working
46
47 172 distance of 15 mm using a beam energy of 25 kV. Two modes of mapping were used: 7 thin
48
49 173 sections underwent dot mapping at a 3 μm pixel size; 3 mounts and 1 thin section underwent and
50
51 174 high-resolution mapping at a 5 μm pixel size. Phase maps were produced from output BSE and
52
53 175 elemental X-ray maps using parameterised X-ray intensity brackets based on the chemistry of the
54
55
56
57
58
59
60

176 known phases. Modal compositions have been calculated as an average phase area fraction of
177 two to three thin sections or mounts for each of the main lithologies.

178 **Quantitative analysis of mineral compositions**

179 BSE imaging and quantitative geochemical analyses using energy dispersive spectroscopy (EDS)
180 of minerals have been carried out on the TESCAN VEGA3 SEM at the Centre for Microscopy,
181 Characterisation and Analysis (CMCA), The University of Western Australia. Analyses were
182 performed at a working distance of 15 mm, an accelerating voltage of 15 kV and a beam
183 intensity of 16 nA were used. All geochemical analyses were calibrated to an external standard
184 (copper) and major element concentrations were determined to be accurate within ± 2 wt%.

185 Additional quantitative geochemical point analyses and mapping using wavelength
186 dispersive spectroscopy (WDS) were carried out on the JEOL JXA-8530F electron microprobe
187 (EMPA) at the CMCA. All analyses were performed using an accelerating voltage of 15 kV, a
188 beam current of 20 nA and spot size of 5 μm .

189 Amphibole and mica compositions were acquired using the following analysing crystals: TAP
190 for Si $K\alpha$, Al $K\alpha$, Na $K\alpha$, and Mg $K\alpha$; PETJ for Ca $K\alpha$, Cl $K\alpha$ and K $K\alpha$; LiF for Mn $K\alpha$ and Fe
191 $K\alpha$; and LiFH for Ti $K\alpha$ and Cr $K\alpha$. Counting time was 30 s for all elements. Scapolite point
192 analyses and element distribution maps were acquired using the following analysing crystals:
193 TAP for Si $K\alpha$, Al $K\alpha$, Na $K\alpha$, and Mg $K\alpha$; PETJ for Ca $K\alpha$ and K $K\alpha$; LiF for Ti $K\alpha$ and Fe $K\alpha$;
194 and PETH for S $K\alpha$, Cl $K\alpha$ and P $K\alpha$. For these analyses the counting time was 20 s for all
195 elements. The standards employed were commercially available silicates, oxides, and metals.
196 Mean atomic number background corrections were employed throughout (Donovan & Tingle,
197 1996). Unknown and standard intensities were corrected for dead time and the ZAF algorithm
198 was used for matrix absorption (Armstrong, 1988). On-peak interference corrections were

1
2
3 199 applied as appropriate (Donovan *et al.*, 1992). Detection limits ranged from 60 ppm for Cl to 370
4
5 200 ppm for FeO.
6
7

8 201 Weight percent oxide data were recalculated into cations per formula unit for individual
9
10 202 minerals, using 6 oxygens for diopside, 12 oxygens for garnet, 8 oxygens for plagioclase, 24
11
12 203 oxygens for scapolite, 23 oxygens for amphibole, 12.5 oxygens for clinozoisite and zoisite, and
13
14 204 11 oxygens for biotite. Amphibole was classified according to the scheme proposed by
15
16 205 Hawthorne *et al.* (2012) using the spreadsheet of Locock (2014). In general, the calculation of
17
18 206 and presentation of scapolite compositional data follows Porter and Austrheim (2017). The
19
20 207 meionite component of scapolite was calculated using: $100 \times \text{Ca} / (\text{Ca} + \text{Na})$. The equivalent
21
22 208 anorthite component of scapolite was calculated using: $100 \times (\text{Al} - 3) / 3$. The amount of C in
23
24 209 scapolite was calculated using: $C_A = 1 - S_A - \text{Cl}_A$.
25
26
27
28

29 210 **Whole rock chemical analysis**

30
31
32 211 Eight samples underwent density measurements by weighing fist-sized specimen in air and water
33
34 212 prior to whole rock analysis at Bureau Veritas Minerals Pty Ltd, Perth, Australia. Samples were
35
36 213 crushed and then pulverised in a vibrating disc pulveriser. SiO₂, TiO₂, Al₂O₃, Fe₂O₃, MgO, CaO,
37
38 214 Na₂O, K₂O, SO₃, Cu and Cl contents were determined by X-ray fluorescence (XRF)
39
40 215 spectrometry on oven dry samples. Loss on ignition (LOI) was determined by heating the oven
41
42 216 dry (105 °C) sample material to 1000 °C using a robotic thermogravimetric analyser (RTGA).
43
44 217 FeO was determined volumetrically. Carbon was determined by total combustion analysis. The
45
46 218 pulverised samples were cast u
47
48
49
50 219 sing a 66:34 flux with 4% LiNO₃ added to form a glass bead. Fused beads were analysed by
51
52 220 Laser Ablation Inductively Coupled Plasma Mass Spectrometry (LA-ICP-MS) for trace and rare
53
54 221 earth element concentrations of Ti, La, Ce, Pr, Nd, Sm, Eu, Gd, Tb, Dy, Ho, Er, Tm, Yb and Lu.
55
56
57
58
59
60

1
2
3 222 The granulite, amphibolite and strained amphibolite compositions represent an average of 2
4
5 223 analyses from separate samples, whereas the compositions of the amphibolite and leucocratic
6
7 224 domains of the shear zone are based on 1 analysis each. The indicated error represents the
8
9 225 combined sample variability and analytical uncertainty where more than 1 sample has been
10
11 226 measured. Where only one sample has been analysed, the error reflects the analytical uncertainty
12
13 227 only. The H₂O concentration is calculated from the LOI minus measured C (as CO₂) and SO₃.
14
15 228 All Fe is considered as Fe₂O₃, noted as Fe^{tot}, for evaluation of its relative concentration changes.
16
17
18
19

20 229 **Shear zone lithology composition**

21
22 230 Due to the relatively wide spacing of compositionally distinct layers, the bulk composition of the
23
24 231 shear zone was obtained by re-integrating the compositions of individual layers instead of
25
26 232 analysing an unrealistically large sample. This was achieved through a combination of whole
27
28 233 rock geochemistry and image analysis. Four separate images of the shear zone outcrop were
29
30 234 analysed using Image-J (Rasband, 1997-2014) to quantify the proportion of dark to light
31
32 235 components using standard thresholding. The separate amphibolite and leucocratic domain
33
34 236 whole rock chemical analyses were then combined based on the calculated average proportions
35
36 237 of 54±3% amphibolite and 46±3% leucocratic domains.
37
38
39
40

41 238 **Thermodynamic modelling**

42
43
44 239 Thermodynamic modelling was undertaken using the software THERMOCALC 3.45 (Powell &
45
46 240 Holland, 1988) and the ‘metabasite set’ of activity-composition (a-X) models (Green *et al.*, 2016
47
48 241 and references therein), calibrated for use with version 6 of the dataset of Holland and Powell
49
50 242 (2011). Solution models used are clinoamphibole (*hb*; Green *et al.*, 2016), clinopyroxene (*dio*, *o*;
51
52 243 Green *et al.*, 2016), epidote (*ep*; Holland & Powell, 2011), garnet (*g*; White *et al.*, 2014),
53
54 244 muscovite (*mu*; White *et al.*, 2014), biotite (*bi*; White *et al.*, 2014), ternary feldspar (*pl*; Holland
55
56
57
58
59
60

1
2
3 245 & Powell, 2003), and tonalitic ‘metabasite’ melt (*L*; Green et al., 2016). Mineral abbreviations
4
5 246 follow solution models where applicable; elsewhere mineral abbreviations follow Whitney and
6
7
8 247 Evans (2010).
9

10 248 The NCKFMASHTO (Na₂O-CaO-K₂O-FeO-MgO-Al₂O₃-SiO₂-H₂O-TiO₂-Fe₂O₃) system
11
12 249 was used for all thermodynamic models. Uncertainty related to the absolute positions of
13
14
15 250 assemblage field boundaries in any individual phase diagram is around ±0.1 GPa and ±50 °C at
16
17 251 the 2σ level (Powell & Holland, 2008; Palin et al., 2016), although relative uncertainty is lower
18
19 252 when comparing equilibria calculated using the same a–X relations and dataset. Here, individual
20
21 253 P and T conditions are relatively precise to around ±0.02 GPa and ±10 °C (Worley & Powell,
22
23 254 2000). Additional uncertainty is expected due to the model system not considering Mn, which is
24
25 255 known to expand the stability of garnet-bearing assemblages in metapelitic rock compositions
26
27 256 (White *et al.*, 2014). As there are currently no Mn solution models for metabasic rocks, it is
28
29 257 unclear whether Mn would have the same effect on the modelled garnet stability fields. Based on
30
31 258 metapelitic model systems and the relatively low concentration of MnO in the studied rocks
32
33 259 (~0.05%; Table 1), expansion of the garnet stability field towards lower pressure may be in the
34
35 260 order of 0.1 GPa. Conversely, no effect on the temperature of garnet stability is expected (White
36
37 261 *et al.*, 2014).
38
39
40
41
42

43 262 T–X_{H₂O} modelling of the amphibolite composition was undertaken to obtain constraints
44
45 263 on the amount of water present at equilibrium conditions. The observed amphibolite assemblage
46
47 264 was not stable at the measured bulk rock H₂O content (0.26 wt%), indicating that the amount of
48
49 265 water present during rock equilibration was not the same as the amount now mineralogically
50
51 266 bound, suggesting that excess water was lost during the exhumation. Stability of the amphibolite
52
53 267 mineral assemblage, using 3 modal% zoisite (see results), is obtained by a relative H₂O content
54
55
56
57
58
59
60

1
2
3 268 increase of 110-135% (0.77-0.91 wt%). A 120% increase in H₂O was used for P–T modelling of
4
5 269 the amphibolite (0.84 wt%) as this gave the best consistency with the P–T conditions provided
6
7 270 by previous estimates. This procedure was repeated for the amphibolite and leucocratic domains
8
9 271 of the shear zone lithology and the results are used for the calculation of P–T and P–X
10
11 272 pseudosections for the relative lithologies.
12
13
14

15 273 **RESULTS**

16 274 **General description of lithologies**

17
18 275 In the following, representative samples of the main lithologies are described according to their
19
20 276 mineralogical assemblage and microstructural features. In general, minerals can be divided into
21
22 277 two categories (1) medium-grained (500 µm – 5 mm) anhedral, equi-granular grains in the
23
24 278 granulite, and, (2) fine-grained minerals (< 500 µm) in the amphibolite and leucocratic domains
25
26 279 as well as along grain boundaries and fractures in the granulite. For ease of description in the
27
28 280 later sections, granulite that has undergone significant alteration (i.e. when the rock contains less
29
30 281 than 30% clear feldspar: Fig. 2c) but still preserves relic pyroxene and garnet and an overall
31
32 282 granoblastic texture is referred to as altered granulite.
33
34
35
36
37
38
39

40 283 *Granulite*

41
42
43 284 Although partially altered, the granulite preserves more than 80% clear feldspar in outcrop (Figs
44
45 285 1c, d and 2a) and is the closest representation of the precursor lithology. The assemblage
46
47 286 comprises plagioclase (An₅₈) (70%), garnet (17%), diopside (9%), and scapolite (2%). Within the
48
49 287 plagioclase dominated matrix, diopside grains form elongated clusters decorated by irregular
50
51 288 coronas of garnet. Fine-grained amphibolite-facies minerals occurring along grain boundaries
52
53
54
55
56
57
58
59
60

289 account for less than 2% of the rock. Grain boundary phases include amphibole, clinozoisite,
290 zoisite, kyanite, biotite, chlorite, plagioclase, K-feldspar, muscovite, and quartz.

291 *Altered granulite*

292 The altered granulite is characterised by a greater extent of fine-grained minerals present as
293 inclusions within the granulitic plagioclase (An₅₈) and at diopside, garnet and plagioclase grain
294 boundaries (Fig. 2c). The assemblage comprises plagioclase (An > 40) (69%), garnet (13%),
295 diopside (9%), and scapolite (2%). Fine-grained minerals occurring along grain boundaries form
296 the same assemblage as in the granulite, however, here they constitute 7% of the rock (Fig. 2c;
297 Fig. 3).

298 In both the granulite and the altered granulite, the spatial distribution of fine-grained (<
299 50 µm in diameter) amphibolite-facies minerals is highly dependent on the chemistry of the
300 granulite host mineral (Figs. 2a-c and 4a, b). Diopside is replaced by a fine-grained assemblage
301 of Mg-hornblende, quartz, clinozoisite, and rutile, whereas garnet is replaced by pargasite,
302 kyanite and plagioclase. Primary plagioclase (An₅₈) is replaced by secondary plagioclase (An₆₈₋₈₂)
303 with inclusions of zoisite, kyanite, and quartz.

304 *Amphibolite*

305 The amphibolite is defined by the complete disappearance of garnet and pyroxene and is
306 composed of less than 30% clear feldspar (Fig. 1c). This lithology consists of a fine-grained
307 assemblage of plagioclase (An > 40) (47%), amphibole (43%), zoisite (3%), kyanite (2%), and
308 biotite (1%) with minor amounts (< 1% each) of clinozoisite, quartz, carbonate, scapolite, biotite,
309 quartz, pyrite, and rutile (Figs 2d and 3). This assemblage is present as two domains: (1)
310 plagioclase and (2) amphibole domains. Plagioclase domains (1) form the matrix of the rock and

1
2
3 311 consist of plagioclase that is partially recrystallized to finer grained aggregates containing
4
5 312 abundant zoisite, kyanite, and quartz inclusions. In addition to the abundant inclusions,
6
7 313 plagioclase in the amphibolite displays reverse zoning, exhibiting relative An-depletion (An_{41-54})
8
9 314 in the inclusion free cores and An-enrichment (An_{64-88}) around inclusions and at grain rims.
10
11

12
13 315 Amphibole domains (2) form discontinuous small (1-2 mm) augen-shaped lenses to
14
15 316 larger (5-10 mm wide) discontinuous lenses. Amphibole domains are more variable in
16
17 317 composition. The compositional variability in amphibole domains is a consequence of the
18
19 318 clustering of secondary phases according to the distribution of the pre-existing phases (Fig. 4c).
20
21 319 Within these domains, clusters of fine-grained (20 – 200 μm) Mg-hornblende, quartz, carbonate,
22
23 320 rutile, and pyrite mimic the geometry of the diopside (Fig. 2a-d). Similarly, the garnet
24
25 321 replacement assemblage, as described for the altered granulite, consists of pargasite, kyanite and
26
27 322 plagioclase with the addition of biotite (Fig. 4c).
28
29
30

31 323 *Strained amphibolite*

32
33
34
35 324 The strained amphibolite occurs within the zone of parallel fabric bordering the shear zone (Fig.
36
37 325 1b). It consists of plagioclase ($An > 40$) (59%), amphibole (18%), zoisite (8%), clinozoisite
38
39 326 (3%), quartz (3%), kyanite (2%), chlorite (2%), scapolite (2%) muscovite (1%), and minor
40
41 327 amounts ($< 1\%$ each) of biotite and rutile (Fig. 2e and 3). The increased quartz component in this
42
43 328 lithology is attributed to the presence of foliation sub-parallel quartz domains. Outside of the
44
45 329 quartz domains, four separate compositional domains can be distinguished within the strained
46
47 330 amphibolite: (1) plagioclase-pure domains (Fig. 2e(i)), (2) plagioclase-zoisite domains (Fig,
48
49 331 2e(ii)), (3) amphibole domains (Fig. 2e(iii)) and (iv) plagioclase-amphibole domains (Fig.
50
51 332 2e(iv)).
52
53
54
55
56
57
58
59
60

1
2
3 333 Plagioclase-pure domains (1) are of similar composition to the plagioclase domains in the
4
5 334 amphibolite, consisting primarily of recrystallized plagioclase with minor amounts of zoisite,
6
7 335 kyanite and quartz. Comparatively, plagioclase-zoisite domains (2) contain an increased
8
9 336 abundance and larger laths of zoisite and kyanite. Amphibole domains (3) consist of almost pure
10
11 337 amphibole with minor amounts of quartz, zoisite, clinozoisite and biotite. Plagioclase-amphibole
12
13 338 domains (4) are unique to the strained amphibolite and consist of a dispersed distribution of
14
15 339 plagioclase, zoisite and amphibole.
16
17
18
19

20 340 *Shear zone lithology*

21
22
23 341 The shear zone lithology exhibits divisible compositional banding defined by the cm-scale
24
25 342 interlayering of leucocratic domains with amphibolite. Within the leucocratic domains, quartz
26
27 343 domains are also observed as discrete foliation-parallel bands.
28
29
30

31 344 The amphibolite domain within the shear zone consists of plagioclase (59%), amphibole
32
33 345 (27%), clinozoisite (4%), zoisite (3%), kyanite (2%), scapolite (2%), and minor amounts (1%
34
35 346 each) of quartz, biotite, muscovite, rutile, and chlorite (Figs. 2f and 3). The amphibolite domain
36
37 347 can be further divided into subdomains: (1) plagioclase and (2) amphibole subdomains. These
38
39 348 two subdomains compositionally resemble the plagioclase and amphibole domains of the
40
41 349 amphibolite (Fig. 2d), however, the bands of amphibole in the shear zone form much more
42
43 350 elongate sigmoidal lenses (Fig. 2f).
44
45
46

47 351 Leucocratic domains consist of plagioclase (74%), zoisite (6%), amphibole (5%),
48
49 352 scapolite (5%), clinozoisite (4%), biotite (2%), and minor amounts (< 1% each) of quartz,
50
51 353 kyanite, chlorite, muscovite, and rutile (Figs 2g and 3). The mineralogy and microstructure of
52
53 354 these domains are largely consistent with the plagioclase-zoisite domains of the strained
54
55
56
57
58
59
60

1
2
3 355 amphibolite (Fig. 2e(ii)) but with the addition of foliation-parallel stringers of quartz, biotite,
4
5 356 clinzoisite, and muscovite (Fig. 2g(i)). Within the stringers rare highly elongate amphiboles
6
7
8 357 may be observed (Fig. 2g(ii) and 4e).

9
10 358 Quartz-rich domains within the shear zone lithology occur exclusively within leucocratic
11
12 359 domains. The quartz-rich domains consist of plagioclase (53%), zoisite (29%), quartz (9%),
13
14 360 kyanite (3%), scapolite (3%), clinzoisite (1%), and minor amounts (< 1% each) of biotite,
15
16 361 muscovite and rutile (Fig. 2h and 3).

20 362 **Local quartz enrichment**

21
22
23 363 Localised quartz enrichment occurs in the granulite, altered granulite, the strained amphibolite
24
25 364 and within leucocratic domains of the shear zone (Figs 2 and 5). In the least altered granulite,
26
27 365 local quartz enrichment occurs along fractures (Figs. 1d and 2b). The fractures are lined by a
28
29 366 200-600 μm wide assemblage of quartz, albite-oligoclase, bytownite and biotite (Figs. 2b(i) and
30
31 367 5a). Quartz along the fracture forms aggregates of 50 to 150 μm grains with planar-curved
32
33 368 quartz-quartz and quartz-albite-oligoclase grain boundaries, commonly meeting at 120° triple
34
35 369 junctions (Fig. 5b). Smaller (5 to 50 μm) quartz and albite-oligoclase grains and quartz grain
36
37 370 aggregates are dispersed within a network of fine-grained (10 to 20 μm) bytownite and biotite.
38
39 371 Quartz and albite-oligoclase grain boundaries in contact with this fine-grained network are
40
41 372 deeply embayed.

42
43
44 373 The alteration haloes of these fractures are evidenced by extensive replacement of the
45
46 374 host plagioclase by an assemblage consisting of zoisite, quartz, and kyanite \pm muscovite (Fig.
47
48 375 5a). Zoisite, quartz and kyanite all occur as 5-20 μm anhedral grains dispersed within
49
50 376 plagioclase. However, with increasing proximity to the fractures, zoisite becomes more angular
51
52 377 and lath-like. Zoisite forms grains up to 1 mm in length closest to the fracture. Where the
53
54
55
56
57
58
59
60

1
2
3 378 alteration halo dissects diopside and garnet, the assemblage consists predominantly of
4
5 379 amphibole, with minor plagioclase, clinozoisite, zoisite, and biotite (Fig. 2b(i)).
6
7

8 380 Additional quartz-lined fractures are observed within the altered granulite (Fig. 5c). The
9
10 381 assemblage within these fractures comprises quartz, oligoclase, bytownite, scapolite, and
11
12 382 tschermakite \pm calcite. Quartz-quartz boundaries are curved-planar, commonly meeting at 120°
13
14 383 triple junctions. Additionally, quartz shares planar to gently curved boundaries with oligoclase,
15
16 384 scapolite, and tschermakite. Tschermakite forms tabular well-faceted to slightly rounded grains
17
18 385 with 50 to 150 μm in diameter. Quartz grain boundaries are also embayed when in contact with
19
20 386 bytownite, but to a lesser degree compared to grain boundaries with albite-oligoclase.
21
22
23
24

25 387 A 2-3 mm wide foliation sub-parallel quartz domain is observed within the strained
26
27 388 amphibolite (Fig. 5d). This layer has a distinct mineralogy in comparison to the surrounding
28
29 389 amphibolite (Fig. 2e). Quartz occurs as foliation-parallel aggregates of 100 to 200 μm grains and
30
31 390 as dispersed 20 to 50 μm cusped grains (Fig. 5d and e) in a matrix of muscovite, biotite, and
32
33 391 oligoclase. Muscovite exhibits sharp and irregular K- and Mg-poor rims (Fig. 5e), associated
34
35 392 with a bright phase, most likely either zircon, rutile, or pyrite, that is apparent along grain
36
37 393 boundaries and in interstitial voids. An-rich plagioclase (labradorite-bytownite) occurs as rims
38
39 394 around oligoclase and is evident at quartz grain boundaries, associated with embayment of the
40
41 395 quartz grain boundary. Associated with the quartz-enriched domain in the strained amphibolite
42
43 396 are 150 to 400 μm long, foliation-parallel laths of zoisite and clinozoisite and kyanite grains with
44
45 397 100 to 200 μm in diameter (Fig. 2e and 5d).
46
47
48
49

50 398 Foliation sub-parallel quartz domains of 3 -5 mm in width are also observed within
51
52 399 leucocratic domains in the shear zone (Fig. 2h and 5f). Here, quartz appears as 100 to 200 μm
53
54 400 grains forming foliation-parallel aggregates as well as dispersed 10 to 100 μm sized grains.
55
56
57
58
59
60

1
2
3 401 Dispersed quartz grains occur as an interstitial phase within foliation-parallel clusters of zoisite
4
5 402 and globular 20 to 50 μm sized kyanite grains. An-poor plagioclase (andesine) rimmed by a
6
7 403 relatively An-rich plagioclase (labradorite) hosts the interstitial quartz, zoisite, and kyanite (Fig.
8
9 404 5f).

13 405 **Amphibole and scapolite mineral chemistry**

14
15 406 Amphibole and scapolite mineral compositions associated with the various lithologies have been
16
17 407 analysed to determine and characterise compositional changes across lithological and structural
18
19 408 transitions; in particular, to trace variations in volatile concentration involved in the amphibolite-
20
21 409 facies alteration and to determine the changes in amphibole composition associated with the
22
23 410 decreased amphibole abundance in the shear zone. Representative amphibolite and scapolite
24
25 411 mineral compositions are reported in Electronic Appendix 1.

30 412 *Amphibole*

31
32
33 413 In all analysed amphibole mineral recalculations, Ca is entirely hosted within the B-site. The Ca-
34
35 414 amphibole plot has been modified accordingly to indicate that A-site occupancy is represented
36
37 415 entirely by Na and K (Fig. 6a). For all measured amphibole compositions, an increase in Cl
38
39 416 concentration is coupled with a decrease in X_{Mg} and an increase in A-site occupancy (Fig. 6a and
40
41 417 b). The most Cl-enriched amphibole (0.02 atoms per formula unit (apfu)) exhibits an X_{Mg} of 0.56
42
43 418 and A-site occupancy of 0.58 and the least Cl-enriched (Cl below detection limit) exhibits an
44
45 419 X_{Mg} of 0.81 and A-site occupancy of 0.06 (Fig. 6a and b).

46
47
48 420 Amphibole at grain boundaries in the least altered granulite occurs as Mg-hornblende and
49
50 421 pargasite (Fig. 6a). Pargasitic amphibole is hosted at diopside-plagioclase and garnet-plagioclase
51
52 422 grain boundaries (Fig 4a). Mg-hornblende occurs within symplectites of quartz, clinozoisite, and
53
54
55
56
57
58
59
60

1
2
3 423 rutile, replacing diopside or as cores within pargasitic grains. Within the granulite amphibole,
4
5 424 X_{Mg} ranges between 0.73-0.85 and Cl concentration is less than 0.002 apfu.
6
7

8 425 Amphibole in the altered granulite varies in composition (Fig. 6a). Pargasite is the most
9
10 426 common composition, occurring in the diopside replacement assemblage as well along fractures
11
12 427 in the plagioclase (Fig. 5c). In association with fractures, Mg-hornblende may appear as cores
13
14 428 within pargasitic grains. Tschermakite and sandanagaite predominantly occur at garnet rims (Fig.
15
16 429 4b). Within the altered granulite, Cl concentration varies (0.001-0.018 apfu, X_{Mg} 0.57-0.79) and
17
18 430 the highest concentration of Cl in amphibole occurs in fractures (0.018 apfu, X_{Mg} =0.57).
19
20
21

22 431 In the amphibolite, the amphibole composition is predominantly Mg-hornblende (Fig.
23
24 432 6a); particularly for smaller (50-100 μ m) grains that occur within the diopside replacement
25
26 433 assemblage (e.g. Fig 4c). Pargasite and sandanagaite are larger (more than 100 μ m) and occur
27
28 434 either as part of the garnet replacement assemblage or at the boundaries between amphibole
29
30 435 clusters and plagioclase (Fig. 4c). Chlorine concentration in the amphibole in the amphibolite is
31
32 436 consistently low, ranging between 0.002 and 0.006 apfu (X_{Mg} 0.63-0.72) (Fig. 6b).
33
34
35
36

37 437 In the strained amphibolite, the amphibole composition is comparatively constant and classifies
38
39 438 as Mg-hornblende (Fig. 6a). The Cl concentration varies between 0.001 and 0.009 Cl apfu with
40
41 439 X_{Mg} 0.62-0.78 (Fig. 6b).
42
43

44 440 The composition of amphibole varies within the shear zone. In leucocratic domains,
45
46 441 where amphibole occurs as highly elongate grains embayed by muscovite and quartz (Fig. 4e),
47
48 442 the composition is dominantly Mg-hornblende (Fig. 6a). These highly elongate amphibole grains
49
50 443 are texturally associated with the alteration of muscovite to biotite (Fig. 4e). Exhibiting a similar
51
52 444 composition to amphibole in the strained amphibolite, amphibole in the leucocratic domains has
53
54 445 a lower Cl concentration (0.003-0.006 Cl apfu) and exhibits a slightly decreased X_{Mg} (0.56-0.69)
55
56
57
58
59
60

1
2
3 446 (Fig. 6b). In the amphibolite domains, amphibole occurs in clusters with quartz, clinozoisite,
4
5 447 zoisite, biotite, and rutile (Fig. 4d). The composition of amphibole in the amphibolite domains
6
7 448 varies between Mg-hornblende, tschermakite, sandanagaite, and pargasite (Fig. 6a). Furthermore,
8
9 449 it has the most consistently increased Cl concentration between 0.002-0.02 Cl apfu and the
10
11 450 lowest X_{Mg} values (0.53-0.70).

15 451 *Scapolite*

16
17
18
19 452 Scapolite is present in all lithologies. In the granulite, scapolite occurs as 150 μm to 5 mm sized
20
21 453 granoblastic grains, either as clusters dispersed throughout the plagioclase matrix or as discrete
22
23 454 veins (Fig. 7c). The chemical composition of scapolite is reported according to the normalised
24
25 455 components of S, Cl, and C in the A-site, the meionite component (X_{Me}) and an equivalent
26
27 456 anorthite component (EqAn; see methods for details on calculation) (Fig. 7a and b). The larger
28
29 457 granoblastic grains in the altered granulite exhibit a consistent core composition with an average
30
31 458 EqAn of 0.62, X_{Me} of 0.73 and A-site occupancy of $S_{0.72}C_{0.28}$. The composition of scapolite in
32
33 459 the least altered granulite was not measured, however, the consistency between these core
34
35 460 compositions and those reported Porter and Austrheim (2017) from nearby granulitic scapolite
36
37 461 veins (EqAn of 0.49-0.54, X_{Me} of 0.61-0.64 and A-site occupancy of $S_{0.68-0.69}C_{0.24-0.25}$; for
38
39 462 location see Fig. 1a) suggest that the cores preserved in the altered granulite are close to original
40
41 463 granulitic composition. At rims of large grains and around zoisite inclusions, the EqAn (0.61)
42
43 464 and X_{Me} (0.72) components are not significantly different. However, the A-site occupancy
44
45 465 becomes slightly more C-enriched with a composition of $S_{0.63}C_{0.36}Cl_{0.01}$ (Fig. 7a (i)). Small
46
47 466 grains (< 60 μm in diameter) occur at the boundaries of large scapolite grains and along fractures
48
49 467 (Fig. 7d). Small grains present at granulitic scapolite grain boundaries have a consistent EqAn
50
51 468 component of 0.57 and X_{Me} of 0.57. In contrast, the A-site occupancy is highly variable $S_{0.09-}$
52
53
54
55
56
57
58
59
60

1
2
3 469 $0.62\text{C}_{0.37-0.89}\text{Cl}_{0.01-0.02}$ (Fig. 7a (ii)). Small grains in fractures have a comparatively consistent C
4
5
6 470 and Cl-rich composition of $\text{S}_{0.10}\text{C}_{0.87}\text{Cl}_{0.04}$ and slight Na-enrichment with an EqAn of 0.48 and
7
8 471 X_{Me} of 0.58 (Fig. 7a: fracture).

9
10 472 In the amphibolite, scapolite forms aggregates of similar shape and size to the precursor
11
12 473 granulitic scapolite (Fig. 7e). However, the A-site occupancy of $\text{S}_{0.03-0.16}\text{C}_{0.83-0.96}\text{Cl}_{0.01-0.02}$ is
13
14 474 relatively C-rich. The EqAn component is 0.53-0.58 and X_{Me} is 0.66-0.71, only slightly lower
15
16 475 than that of the granulitic scapolite.

17
18
19
20 476 Scapolite in the strained amphibolite and the shear zone lithology are similar in
21
22 477 composition (Fig. 7a and b). The EqAn component of scapolite in the strained amphibolite
23
24 478 ranges from 0.55-0.62 and X_{Me} ranges between 0.64-0.68, while the A-site occupancy shows a
25
26 479 variation of $\text{S}_{0.21-0.42}\text{C}_{0.57-0.78}\text{Cl}_{0.01-0.02}$. Scapolite in the shear zone lithology is more variable in
27
28 480 composition with an EqAn component that varies from 0.49-0.57, X_{Me} between 0.60-0.69, and
29
30 481 the A-site occupancy of $\text{S}_{0.06-0.43}\text{C}_{0.56-0.91}\text{Cl}_{0.01-0.03}$.

31 482 **Mass balance across fracture alteration haloes**

32
33
34
35 483 Mass transfer associated with fractures and their alteration haloes were assessed using
36
37 484 quantitative major element maps of the granulitic plagioclase, the fracture alteration halo, and the
38
39 485 fracture assemblage in the granulitic plagioclase. The integrated average compositions of each of
40
41 486 the map areas are compared to quantify whether the amphibolite-facies hydration is associated
42
43 487 with an influx of (non-volatile) major elements. Maps and the total composition of the map areas
44
45 488 are given in Electronic Appendix 2a and b, respectively.

46
47
48
49 489 For the map areas only SiO_2 , Al_2O_3 , CaO , Na_2O , and K_2O were present in concentrations
50
51 490 above the detection limit. All detectable element oxide concentrations overlap within the
52
53
54
55
56
57
58
59
60

1
2
3 491 uncertainty and are consistent with stoichiometric plagioclase. SiO₂ and Al₂O₃ make up the
4
5 492 major component of the map areas at 53.9 wt% and 30.0 wt% in the granulitic plagioclase, 53.9
6
7
8 493 wt% and 29.8 wt% in the alteration halo, and 54.9 wt% and 29.9 wt% in the fracture. CaO,
9
10 494 Na₂O, and K₂O can be simplified as relative proportions of An and Or-components in the map
11
12 495 area. Neither the fracture (An₅₆Or₂) nor the alteration halo (An₅₇Or₂) exhibit a significant change
13
14 496 in composition in comparison to the granulitic plagioclase (An₅₈Or₂).
15
16

17 497 **Changes in whole rock composition related to hydration and deformation**

18 19 20 21 498 *Mass balance*

22
23
24 499 The whole rock chemistry of the main amphibolite-facies lithologies amphibolite, amphibolite
25
26 500 domains, the leucocratic domains, and the re-integrated shear zone lithology is presented in the
27
28 501 form of mass change relative to the precursor granulite, based the constant mass reference frame
29
30 502 (Grant, 1986). The strained amphibolite is excluded from the mass-balance calculation due to its
31
32 503 compositional heterogeneity (e.g. Fig. 2e), which may result in an erroneous interpretation of
33
34 504 mass change. Using the constant mass reference frame negates the need to define one or more
35
36 505 immobile elements, hence eliminating the uncertainty involved with choosing the correct
37
38 506 geochemical reference frame for a metasomatised system (Ague & Van Haren, 1996). The
39
40 507 choice of using fixed mass is further verified by the only minor hydration-related density
41
42 508 changes from 2.87 g/cm³ in the granulite to 2.86 g/cm³ in the amphibolite. The amphibolite
43
44 509 domain has a density of 2.89 g/cm³ and the leucocratic domain has a density of 2.80 g/cm³.
45
46
47 510 Whole rock compositions and densities are given in Table 1.
48
49
50

51
52 511 *Major elements.* Similar distributions are observed for Al₂O₃ and CaO, both showing
53
54
55 512 only very minor mass change, decreasing in the amphibolite (-2% and -3%) and amphibolite
56
57
58
59
60

1
2
3 513 domains (-4% and -2%), but increasing in the leucocratic domains (+10% and +5%) and the re-
4
5 514 integrated shear zone lithology (+2% and +1%) (Fig. 8). SiO₂ and Na₂O are similarly coupled,
6
7 515 increased in the leucocratic domains (+2% and +22%), decreased in the amphibolite (-1% and -
8
9 516 2%) and the amphibolite domains (-4% and -10%) accounting to an overall loss of SiO₂ (-1%)
10
11 517 and gain of Na₂O (+5%) in the re-integrated shear zone lithology. Mass gains of K₂O are
12
13 518 exhibited in the amphibolite domains (+21%) and the re-integrated shear zone lithology (+9%),
14
15 519 while losses are observed in the amphibolite (-12%) and the leucocratic domains (-6%). In
16
17 520 comparison to the other major elements, Fe^{tot} and MgO show much greater mobility. An increase
18
19 521 of Fe^{tot} concentration occurs in the amphibolite (+11%) and the amphibolite domains (+50%) but
20
21 522 decreased concentrations occur in leucocratic domains (-75%) and the re-integrated shear zone
22
23 523 lithology (-7%), relative to the granulite. Similarly, the MgO concentration is increased in the
24
25 524 amphibolite (+16%) and amphibolite domains (+24%), but exhibits loss in the leucocratic
26
27 525 domains (-87%) and the re-integrated shear zone lithology (-27%) (Fig. 8).
28
29
30
31
32
33

34 526 *Volatile elements and Cl.* Water is increased in all amphibolite-facies lithologies relative
35
36 527 to the granulite (Fig. 8). The amphibolite and amphibolite domains exhibit the same relative
37
38 528 increase in H₂O (both +280%). The leucocratic domains of the shear zone exhibit the highest
39
40 529 concentration of H₂O, increased by +400%, producing a re-integrated shear zone lithology H₂O
41
42 530 mass gain of +340%. Chlorine increases by over +3000% in amphibole-bearing lithologies, with
43
44 531 the strongest increase observed in the amphibolite domains (+6200%; Fig. 8). In the leucocratic
45
46 532 domain, Cl concentrations are 500% higher than in the granulite. The SO₃ concentration is
47
48 533 uniformly increased across all amphibolite-facies lithologies, varying from +180% in the
49
50 534 amphibolite domains to +190% in the amphibolite. In contrast, CO₃ only exhibits increased
51
52
53
54 535 concentration in the amphibole-bearing rocks. The largest increase is observed in the amphibolite
55
56
57
58
59
60

1
2
3 536 (+100%), whereas the amphibolite domains exhibits only a small increase (+33%). The increase
4
5 537 in CO₃ in the amphibolite domains seems balanced by a mass loss in the leucocratic domains (-
6
7
8 538 33%), producing an overall mass change of +3% CO₃ in the re-integrated shear zone lithology.
9

10 11 539 *Rare earth element patterns*

12
13
14 540 Rare earth element (REE) concentrations are presented here normalised to chondrite
15
16 541 (McDonough & Sun, 1995) (Fig. 9). The REE patterns are presented for the purpose of
17
18 542 evaluating whether there is any significant REE fractionation across the hydration and
19
20 543 deformation interface, due to either original compositional variation or mass transfer during
21
22 544 metamorphism.
23
24
25

26 545 Changes in concentration of REE across the shear zone interface result in only very
27
28 546 minor differences in patterns. All lithologies exhibit steeply dipping REE patterns with a marked
29
30 547 Eu anomaly. The Eu anomalies for each lithology a broadly similar with the largest anomaly
31
32 548 observed in the amphibolite (Eu/Eu* = 4.22) and the smallest in the amphibolite domains
33
34 549 (Eu/Eu* = 2.48). The fractionation of REE is similar for the granulite (La/Yb_N = 8.47), the
35
36 550 strained amphibolite (La/Yb_N = 7.59), and the amphibolite domains (La/Yb_N = 8.92). The
37
38 551 amphibolite is slightly more fractionated (La/Yb_N = 12.85), owing to an apparent loss of medium
39
40 552 to heavy REE relative to the granulite. By comparison, the leucocratic domains appear slightly
41
42 553 more fractionated (La/Yb_N = 20.3) due to a significant increase of light REEs, without an
43
44 554 increase in M-HREE, relative to the granulite.
45
46
47
48
49

50 555 **P-T-X_{H2O} constraints on amphibolite formation and the shear zone**

51
52 556 The amphibolite, the amphibolite domains and leucocratic domains have been modelled in T-
53
54 557 X_{H2O} pseudosections (Fig. 10a-c) to constrain the amount of fluid present during equilibration of
55
56
57
58
59
60

1
2
3 558 the observed assemblages. For each of the presented models, the $X_{\text{H}_2\text{O}}$ composition is the
4
5 559 measured H_2O content at X_0 and a near 400% increase of molar% H_2O at X_1 . Epidote
6
7 560 composition is consistent with the observed composition ($X_{\text{czo}} > 0.95$) within all modelled
8
9 561 conditions. Complete P–T pseudosections for each of the lithologies presented in Fig. 10 are
10
11 562 provided in Electronic Appendix 3.
12
13
14

15 563 For both amphibolite assemblages, T– $X_{\text{H}_2\text{O}}$ modelling indicates an increased H_2O
16
17 564 component during equilibration of the observed assemblage relative to the measured amount
18
19 565 (Fig. 10a and b). In both the amphibolite and amphibolite domain T– $X_{\text{H}_2\text{O}}$ sections the stability
20
21 566 of the garnet-absent mineral assemblage is tightly constrained by the garnet-producing reaction,
22
23 567 occurring at predominantly lower T– $X_{\text{H}_2\text{O}}$ compositions. The H_2O component is constrained by
24
25 568 zoisite modal isopleths at 3 modal% for both amphibolite lithologies (Fig. 3). For both
26
27 569 lithologies, H_2O concentration estimates represent a range that is close to the maximum ambient
28
29 570 temperature estimate of 730°C while remaining below the solidus. At temperatures between 675°C –
30
31 571 720°C the amphibolite has an estimated 0.77–0.91 wt% H_2O and at temperatures between 670°C –
32
33 572 715°C the amphibolite domain has an estimated 0.95–1.10 wt% H_2O . The median values of 0.84
34
35 573 wt% H_2O for the amphibolite and 1.03 wt% H_2O for the amphibolite domains have been taken to
36
37 574 produce the mineral stability fields in P–T space (Fig. 10d). In contrast to the amphibolite
38
39 575 assemblages, the leucocratic domain assemblage (6 modal% zoisite) is stable at the measured
40
41 576 H_2O content (X_0 ; 0.48 wt%) at $\sim 705^\circ\text{C}$ (Fig. 10c). When modelled in P–T space, all lithologies
42
43 577 produce mineral stability fields that are in agreement with previous estimates of 590°C – 730°C and
44
45 578 1.0–1.4 GPa for the conditions of amphibolite-facies metamorphism that are derived from
46
47 579 mineral thermobarometry (Fig. 10d) (see also Moore et al., 2020 and references therein). The
48
49 580 stability of the assemblages of the individual lithologies overlap at peak conditions of 720°C and
50
51
52
53
54
55
56
57
58
59
60

1
2
3 581 1.14 GPa. At these conditions, the calculated water activities ($\alpha_{\text{H}_2\text{O}}$) for the Thermocalc reactions
4
5 582 are 0.63 for the amphibolite, 0.77 for the amphibolite domains and 0.87 for the leucocratic
6
7
8 583 domain assemblages.

10 584 **Modelling of shear zone mineralogical distribution in P-X space**

11
12
13 585 Based on the bulk H_2O content derived from the T- $X_{\text{H}_2\text{O}}$ pseudosection calculations, we evaluate
14
15 586 in P-X space whether the mineral distribution in the shear zone is consistent with the attainment
16
17
18 587 of thermodynamic equilibrium during or subsequent to mass transfer, and whether the
19
20 588 segregation of the two distinct shear zone lithologies occurred at the same P-T conditions (Fig.
21
22 589 11a). The P-X pseudosection has been fixed at 720°C, consistent with the observed assemblage
23
24
25 590 and Zr-in-rutile thermometry (Fig. 10d). This temperature represents an upper limit and was
26
27 591 inferred to reflect near peak metamorphic conditions. For the P-X sections, X_0 represents the
28
29 592 amphibolite domain composition and X_2 the leucocratic domain composition as in Fig. 10d and
30
31 593 Electronic Appendix 3.

32
33
34 594 Additional mass-balance calculations, using constant mass as the reference frame, for the
35
36 595 two shear zone lithologies relative to the re-integrated shear zone lithology and the re-integrated
37
38 596 shear zone lithology relative to the granulite are presented within Fig. 11a, to enable comparison
39
40 597 with partial melt calculations. The leucocratic and amphibolite domain compositions indicate a
41
42 598 close to balanced exchange of Na_2O , H_2O , K_2O , Cl, Fe^{tot} , and MgO between the two lithologies
43
44 599 (Fig. 11a). The amphibolite domain is relatively depleted in Na_2O (-14%) while exhibiting mass
45
46 600 gains in H_2O (+33%), K_2O (+11%), Cl (+71%), Fe^{tot} (+62%), and MgO (+70%). In the
47
48 601 leucocratic domains, the reciprocal trend is observed, here Na_2O is gained (+16%) while H_2O (-
49
50 602 38%), K_2O (-13%), Cl (-84%), Fe^{tot} (-73%), and MgO (-82%) are relatively depleted.
51
52
53 603 Discrepancies of more than 10% mass change of Fe^{tot} , MgO, and Cl between the leucocratic
54
55
56
57
58
59
60

1
2
3 604 domain and the amphibolite domains are consistent with the observed total mass loss of Fe^{tot} (-
4
5 605 7%) and MgO (-27%) and mass gain of Cl (+3600%) in the re-integrated shear zone lithology
6
7
8 606 relative to the granulite composition (Fig. 8g and 11a). Furthermore, the depletion of MgO and
9
10 607 Fe^{tot} in the leucocratic domains corresponds with the observed (X_0 : 27%, X_2 : 5%; Fig. 3 and 11c)
11
12 608 and modelled (X_0 : 39%, X_2 : 4%; Fig. 11b) decreased modal abundance of amphibole.

13
14
15 609 As in the T- $X_{\text{H}_2\text{O}}$ pseudosection, equilibrium conditions for the amphibolite domains
16
17 610 assemblage are also constrained in the P-X space by the garnet-in and the zoisite-out reactions to
18
19 611 1.09- 1.19 GPa (X_0 ; Fig. 11a). However, the zoisite modal abundance is only consistent with the
20
21 612 observed value (3%; Fig. 3 and 11c) in the presence of partial melt (1%) in the assemblage
22
23 613 (Figure 11a and b). If the pressure estimate is based on the zoisite 3% modal isopleth, the
24
25 614 stability of the amphibolite domains assemblage is constrained to 1.10 ± 0.04 GPa at X_0 .

26
27
28
29 615 For the leucocratic domains, garnet is not stable at any of the presented P-T conditions
30
31 616 (Fig. 10c and 11a). The stability of the mineral assemblage is instead confined by the muscovite-
32
33 617 out reaction at 1.24 GPa and the zoisite-out reaction at 1.12 GPa. Also, for the leucocratic
34
35 618 domains, the observed zoisite modal abundance (6%) can only be reproduced in the presence of
36
37 619 partial melt (1%) (Fig. 11a and b). Based on the 6% modal isopleth for zoisite the stability of the
38
39 620 assemblage in the leucocratic domains is constrained to 1.14 ± 0.01 GPa at X_2 .

621 **Composition of partial melt approximated from thermodynamic modelling**

622 P-X modelling indicates that partial melt may have been present during at least one stage of
623 metamorphism of the shear zone lithology (Fig. 11a and c). The calculated melt composition is
624 presented for comparison with the observed elemental mobility (Fig. 12 and Electronic Appendix
625 4). As this is an investigation of the composition that would result from hydration-induced
626 melting, a T- $X_{\text{H}_2\text{O}}$ diagram has been constructed for the granulite (Electronic Appendix 3), and

1
2
3 627 melt compositions have been calculated at 720°C and 11 kbar with 1, 5, and 9% melt component.
4
5 628 Based on these estimates the expected mass changes in the solid residuum and the liquid relative
6
7
8 629 to the anhydrous granulite have been calculated.
9

10
11 630 At the low degree of partial melting, the produced melt is primarily a hydrous
12
13 631 aluminosilicate with a composition of ~62% SiO₂, ~16% Al₂O₃, and ~13% H₂O. In terms of
14
15 632 mass change relative to the granulite precursor, melting involved mass gains in the melt
16
17 633 component in Na₂O (9-20%), SiO₂ (23%), K₂O (670-900%), and H₂O (> 10,000%).
18
19

20
21 634 The main compositional change occurring during the partial melting is the fractionation
22
23 635 of H₂O and K₂O into the melt, resulting in a 740-800% mass gain in H₂O and a 38-52% mass
24
25 636 loss of K₂O in the residual solid (Fig. 12). At 1, 5, and 9% partial melt SiO₂, Na₂O, CaO and
26
27 637 Al₂O₃ all exhibit <5% mass loss while FeO and MgO exhibit mass gains of 7-10 and 6-9%,
28
29 638 respectively.
30
31

32 33 639 **DISCUSSION**

34 35 640 **Quartz enrichment on fracture planes**

36
37
38 641 Quartz-lined fractures in the granulite (Fig. 2c) and the quartz-enriched domains within the
39
40 642 strained amphibolite and the leucocratic domains (Fig. 5) are mineralogically and texturally
41
42 643 similar. They are associated with planar aligned clusters of quartz containing abundant zoisite
43
44 644 laths (100 µm – 1mm), particularly in the alteration haloes. The main difference between quartz-
45
46 645 lined fractures and quartz-enriched domains is that the latter are aligned as foliation-parallel
47
48 646 bands (Fig. 2e, h and 5d, f). The mineralogical and textural resemblance of the quartz-lined
49
50 647 fractures and quartz-enriched domains suggests a common origin of these features, with the
51
52
53
54
55
56
57
58
59
60

1
2
3 648 foliation-parallel quartz-enriched domains having undergone further deformation during or after
4
5 649 their formation.
6
7

8 650 Furthermore, the amphibolite mineral assemblage, comprising plagioclase, amphibole,
9
10 651 zoisite, kyanite, clinozoisite, and quartz \pm scapolite \pm biotite (Fig. 2d), is consistent with that of
11
12 652 the fracture alteration haloes in the granulite (Fig. 2c), suggesting that the fractures formed
13
14 653 during initial fluid infiltration or represent pre-existing high permeability pathways that were
15
16 654 later exploited by infiltrating fluids to produce the amphibolite assemblage. Within the shear
17
18 655 zone lithologies, quartz-enriched domains are exclusively found within the leucocratic domains
19
20 656 (Fig. 2). A quartz-enriched domain is also observed in the strained amphibolite, associated with a
21
22 657 higher abundance of zoisite and plagioclase in comparison to the amphibolite (Figs. 2d, e and 3).
23
24 658 The association between quartz-enriched domains and increased plagioclase and zoisite
25
26 659 abundance suggests that they may be integral to understanding the processes driving the
27
28 660 formation of leucocratic domains, and hence the differentiation of the shear zone lithology. The
29
30 661 intimate interlayering of the leucocratic and the amphibolite domains in the shear zone lithology
31
32 662 suggests that the quartz-enriched, leucocratic and amphibolite domains formed during the same
33
34 663 metamorphic event. In addition, the observed replacement of amphibole by quartz and biotite
35
36 664 within leucocratic domains (Fig. 4e) indicates that the processes driving the segregation of the
37
38 665 rock into quartz-enriched domains, and by extrapolation, leucocratic and amphibolite domains,
39
40 666 continued after the initial amphibolite-forming hydration event.
41
42
43
44
45
46
47

48 667 **Externally derived elements vs. internal fractionation**

49
50 668 To gain insight into the mechanism of metamorphic differentiation within the shear zone, the
51
52 669 composition of the infiltrating fluid is examined to determine whether the observed
53
54 670 compositional variation of the rock is the result of externally derived major element addition.
55
56
57
58
59
60

1
2
3 671 The whole rock analysis reveals mass gains in H₂O, SO₃, and Cl in all lithologies relative to the
4
5 672 granulite (Fig. 8), indicating that the infiltrating fluid was not purely water. The whole rock mass
6
7 673 gain of Cl in the amphibolite and shear zone lithologies is in agreement with the analysis of fluid
8
9 674 inclusions from quartz veins from the nearby Holsnøy metamorphic complex (for location see
10
11 675 Fig. 1a) (Andersen *et al.*, 1991). The authors report two types of veins, one occurring in the
12
13 676 centre of amphibolite-facies shear zones and another one exhibits alteration haloes in statically
14
15 677 hydrated granulite, i.e. similar to the occurrence of quartz at Fjellsende. Fluid inclusion
16
17 678 compositions from the reported veins are between 2-50 wt% NaCl_{eq} and molar CaCl₂/(CaCl₂ +
18
19 679 NaCl) ratios of 0.28 in the shear zone and 0-0.4 in the smaller veins in the granulite, indicating
20
21 680 the presence of saline fluid during amphibolite-facies metamorphism. The Na and Ca contents of
22
23 681 these fluid inclusions is at odds with the whole rock analysis of this study which indicates no
24
25 682 significant mass gain or loss of those elements across the hydration interface (Fig. 8). Indeed,
26
27 683 quantitative analysis of alteration haloes in plagioclase reveals that there was no significant gain
28
29 684 or loss of plagioclase forming oxides (SiO₂, Al₂O₃, Na₂O, K₂O and CaO) associated with
30
31 685 fracturing and fluid infiltration (Electronic Appendix 2). Other major elements (Fe^{tot}, MgO, and
32
33 686 TiO₂) are below their detection limits and hence did not undergo measurable mass gain
34
35 687 (Electronic Appendix 2). Given the lack of evidence for significant influx of externally derived
36
37 688 Na, Ca, and Si, the reported elevated Na and Ca contents in fluid inclusions (Andersen *et al.*,
38
39 689 1991) is deemed to be most likely the result of local fluid-rock reactions instead of being
40
41 690 characteristic of amphibolitization fluids at a larger scale. Consequently, it is inferred that quartz-
42
43 691 lined fractures associated with the amphibolite-facies event cannot be formed as the result of
44
45 692 precipitation of major element oxides from an infiltrating fluid, and are instead formed as a result
46
47
48
49
50
51
52
53
54
55
56
57
58
59
60

1
2
3 693 of the internal fractionation and recrystallization of the host rock during the infiltration of a Cl-
4
5 694 bearing aqueous fluid.

6
7
8 695 The absence of mass gain is consistent further with the whole rock mass-balance
9
10 696 calculation for the re-integrated shear zone lithology, indicating insignificant major element
11
12 697 gains relative to the granulite (Fig. 8d). There is, however, a considerable loss of MgO in the shear
13
14 698 zone (-27%; Fig. 8d), particularly from the leucocratic domains (Fig. 8c and 11a). This depletion
15
16 699 of MgO is evidenced not only by the mass balance but also by the observed breakdown of
17
18 700 amphibole within these domains (Fig. 4e). The highly elongate nature of the grains and the
19
20 701 protruding neighbouring quartz and mica are indicative of incongruent dissolution of the
21
22 702 amphibole (Wassmann & Stöckhert, 2013). Furthermore, the associated sharp irregular zones of
23
24 703 biotite replacing muscovite indicate mass transport during the breakdown reaction. Even though
25
26 704 these reactions may be expected during the partial melting of a rock undergoing differential
27
28 705 stress, the modelled patterns of element redistribution via partial melting is inconsistent with the
29
30 706 recorded mass change in the shear zone lithology (Fig. 12). Modelling of partial melting of the
31
32 707 granulite indicates a melt component that should be relatively enriched in SiO₂, Na₂O, and K₂O
33
34 708 and a solid residual component that would be relatively depleted of feldspar forming elements
35
36 709 and enriched in FeO and MgO. Consequently, the redistribution of elements in the shear zone
37
38 710 lithology was by fluid–rock interaction that was also accompanied but not driven-by partial
39
40 711 melting.

41 42 43 44 45 46 47 712 **Reaction mechanism**

48
49
50 713 We infer that dissolution-precipitation is the governing reaction mechanism. This interpretation
51
52 714 is corroborated by textural evidence, including sharp reaction fronts in partially replaced
53
54 715 plagioclase (Fig. 4b and 5c), diopside (Fig. 4a), and garnet (Fig. 4a and c) in the granulite, as

1
2
3 716 well as sharp and irregular compositional fronts in muscovite (Fig. 4e and 5e) and plagioclase
4
5 717 (Fig. 5e) in the amphibolite assemblages (Putnis, 2009). While the thermodynamic modelling
6
7 718 does not indicate that H₂O was in excess during the transformation of the granulite to
8
9 719 amphibolite (Fig. 10a-c and Electronic Appendix 3) the a-X solution models are limited to pure
10
11 720 H₂O fluid compositions and thus cannot preclude the presence of a more compositionally
12
13 721 complex fluid. We argue that the textural evidence alone is sufficient to suggest the presence of
14
15 722 free fluid during the amphibolite-facies metamorphism. Despite the relatively high temperature,
16
17 723 mineral replacement driven by solid-state diffusional modification of phase compositions is
18
19 724 generally slower than mineral replacement by dissolution-precipitation reactions mechanism
20
21 725 (Pattison, 1994, Rubie, 1986), and thus solid-state mechanisms are unlikely to be dominant.
22
23
24
25

26
27 726 Interface-coupled dissolution-precipitation reactions involve three main processes;
28
29 727 dissolution of precursor mineral at the interface, precipitation of reaction products, and diffusive
30
31 728 transport to and from the reaction front (Rutter, 1983, Xia *et al.*, 2009). Whichever of the
32
33 729 processes is the slowest is the rate-limiting step. The assemblages forming the statically hydrated
34
35 730 amphibolite and the quartz-lined fractures exhibit contrasting reaction microstructures. In the
36
37 731 amphibolite and at grain boundaries in the granulite, static replacement of anhydrous granulite-
38
39 732 facies minerals by fine-grained aggregates of amphibolite-facies minerals is evident (Fig. 4a and
40
41 733 b). Amphibolite-facies mineral assemblages maintaining morphological and chemical evidence
42
43 734 of the phases they have replaced in the completely reacted amphibolite (Fig. 4c and d). When
44
45 735 replacement of a mineral during a hydration reaction is pseudomorphic, as is observed in the
46
47 736 amphibolite (Fig. 4c), then it is theorised that the replacement process is rate-limited by
48
49 737 dissolution at the interface (Xia *et al.*, 2009). In contrast, when precipitation is rate-limiting then
50
51 738 solute transport is likely to occur, resulting in mass loss at the dissolution interface.
52
53
54
55
56
57
58
59
60

1
2
3 739 Within the quartz-lined fractures and quartz-enriched domains, there is no evidence for
4
5 740 the direct replacement of host minerals by the newly formed quartz (e.g. mineral inclusions).
6
7
8 741 Furthermore, the clusters of quartz and plagioclase lining the fracture walls, and scapolite and
9
10 742 tschermakite in the fractures exhibit characteristic curved-planar grain boundaries, commonly
11
12 743 forming 120° triple junctions (Fig. 5). This microstructure is indicative of low interfacial energy
13
14
15 744 and characteristic for grain growth from a free fluid (see Vernon, 2018). Consequently,
16
17 745 precipitation must have been decoupled from dissolution, consistent with the presence of
18
19 746 amphibole and biotite as fracture filling in plagioclase (Fig. 5a and c), requiring external MgO
20
21 747 and Fe^{tot}. However, the length scale of mass transport must have been shorter than resolvable at
22
23
24 748 the given sampling resolution (Fig. 8).

25
26 749 In addition to textural evidence for the decoupling of precipitation from dissolution, we
27
28
29 750 also observe distinct chemical compositions of minerals between the statically hydrated
30
31 751 amphibolite and fracture fillings (Fig. 6 and Fig. 7a and b). For example, within the same thin
32
33 752 section, both amphibole and scapolite in fractures in the altered granulite exhibit higher Cl
34
35 753 concentrations in comparison to grains formed by replacement of diopside and garnet in the
36
37
38 754 static amphibolite. Given the systematic relationship between Cl concentration and
39
40 755 microstructure and considering the predominantly aqueous composition of the fluid, it is unlikely
41
42
43 756 that the difference in Cl concentration results from compositional heterogeneity in the infiltrating
44
45 757 fluid. The observed higher fluid inclusion salinity (20-50 wt% NaCl_{eq}) in quartz-lined fractures
46
47 758 in statically hydrated granulite compared with shear zones (2-16 wt% NaCl_{eq}) (Andersen *et al.*,
48
49 759 1991), are more consistent with closed system (mm-cm scale fluid connectivity; Fig. 13d), rock-
50
51
52 760 buffered conditions where H₂O-consuming hydration reactions increase fluid salinity in the
53
54 761 fractures (see also Lamadrid *et al.*, 2017, Markl & Bucher, 1998, Markl *et al.*, 1998).

1
2
3 762 Conversely, the shear zone represents a relatively open system (> cm scale fluid connectivity;
4
5 763 Fig. 13e) allowing for fluid-buffered mineral growth.
6
7

8 764 Given the previous work on fluid inclusions of Andersen *et al.* (1991), it can be argued
9
10 765 that for the thermodynamically modelled lithologies (Fig. 10) the calculated water activity can be
11
12 766 used as a proxy for salinity, as a decreased water activity would be expected where salinity is
13
14 767 increased. The calculated water activity for the equilibrium assemblages was lowest in the
15
16 768 amphibolite ($\alpha_{\text{H}_2\text{O}} = 0.63$), higher in the amphibolite domains ($\alpha_{\text{H}_2\text{O}} = 0.77$) and highest in the
17
18 769 leucocratic domains ($\alpha_{\text{H}_2\text{O}} = 0.87$) (Fig. 10d). These values are consistent with the measured
19
20 770 higher salinity of fluid inclusions within the statically hydrated alteration haloes in comparison to
21
22 771 the shear zone (see above discussion), further supporting the interpretation that formation of the
23
24 772 leucocratic domains was via aqueous fluid-buffered reactions, in comparison to those occurring
25
26 773 during the static hydration of the amphibolite.
27
28
29
30

31 774 The partitioning of Cl into amphibole and scapolite appears to be more effective in
32
33 775 fractures (Fig. 6 and 7) and increased amphibole Cl concentrations are also observed in the
34
35 776 amphibolite domains in comparison to the statically hydrated amphibolite (Fig. 6). The
36
37 777 observation of increased Cl content in amphibole texturally associated with more deformed,
38
39 778 plagioclase-rich lithologies has been described previously (Kullerud, 1996). This author
40
41 779 attributes the Cl enrichment in amphiboles to growth from an evolved, rock-buffered fluid in a
42
43 780 closed system. This model is consistent with that described above for the increased salinity of
44
45 781 fluid inclusions associated with fractures in the granulite and may also explain the increased Cl
46
47 782 content of scapolite and amphibole in fractures (Fig. 6 and 7).
48
49
50
51
52
53
54
55
56
57
58
59
60

783 **Dissolution-precipitation driven mass transfer**

784 Two types of reaction zones can be broadly defined for the amphibolite-facies hydration event;
785 those in which the reaction rate is limited by dissolution (i.e. the amphibolite and the amphibolite
786 domains), and those where precipitation is the rate-limiting step thus enhancing mass transport
787 (i.e. quartz-lined fractures and leucocratic domains). The formation and evolution of these
788 reaction zones is illustrated schematically in Fig. 13.

789 Quartz-enriched domains are texturally and compositionally analogous to quartz-lined
790 fractures, with the exception that, despite being strained, quartz-enriched domains occupy wider
791 zones (3-5 mm) in comparison to quartz-lined fractures (200-600 μm ; Fig. 2b and h). Quartz-
792 enriched domains are thus interpreted as larger versions of quartz-lined fractures, representing a
793 snapshot of the initial amphibolite-facies fluid infiltration (Fig. 13a). After the initial fracturing,
794 the fractures and their damage zones form zones of relatively high permeability. These high
795 permeability zones are of two-fold importance for the distribution of dissolution and
796 precipitation reactions: they allow the influx and mobility of fluid within the unaltered granulite,
797 instigating the amphibolite-facies reactions, and, they allow for locally decreased pore-fluid
798 pressure.

799 In the following section a coupling between the increased permeability around fractures
800 and the reaction mechanism is theorised. For simplicity and consistency with the referenced
801 literature, the following discussion will refer to stress using only normal stress, neglecting the
802 shear stress component. The relevance and intricacies of the application of shear stresses in
803 systems undergoing reaction, maintained by a grain boundary fluid, have been discussed more
804 thoroughly in previous contributions and are beyond the scope of this work (for review see;
805 Wheeler, 2018).

1
2
3 806 Decreased pore-fluid pressure is essential for maintaining differential stresses during
4
5 807 reaction. This is most easily demonstrated by the following equation:

6
7
8 808 (1) $\sigma_{\text{eff}} = \sigma_n - P_f$
9

10
11 809 where σ_{eff} is the effective normal stress, σ_n is the normal stress and P_f is the interconnected pore
12
13 810 fluid pressure (Cox, 2010, Hill, 2015). It follows that as P_f approaches the value of σ_n than σ_{eff}
14
15 811 will be reduced and the tensile strength of the rock may be exceeded, resulting in brittle failure
16
17 812 (Cox, 2010). The maintenance of low pore-fluid pressure is therefore necessary for continued
18
19 813 reaction at high differential stresses. Continued low pore-fluid pressure may be achieved where
20
21 814 high permeability is maintained along zones where the initial damage, fluid infiltration, and
22
23 815 reaction were significant enough to produce weakening and ultimately deformation (Fig. 13b and
24
25 816 e). Conversely, where the reacting volume is closed off to further fluid/mass exchange (Fig.
26
27 817 13d), the volume increase associated with the hydration reactions (Centrella *et al.*, 2015) will
28
29 818 both work to further seal the rock from fluid replenishment and increase the pore-fluid pressure
30
31 819 so that the effective normal stress is subdued.
32
33
34
35
36

37 820 Two endmembers for the conditions under which reactions proceed can be established; (I;
38
39 821 Fig. 13d) where, following initial fluid infiltration, reactions proceed in a closed system under
40
41 822 relatively low differential stress coinciding with dissolution-limited reaction (i.e. the amphibolite
42
43 823 and amphibolite domains) and (II; Fig. 13e) where continued permeability allows for high
44
45 824 differential stresses to be maintained, coinciding with precipitation-limited reaction (i.e. quartz-
46
47 825 lined fractures and leucocratic domains). Based on these scenarios it then follows that there are
48
49 826 two possible key factors that influence the difference in reaction products between each of these
50
51 827 scenarios; (1) the contrasting length-scales of elemental mobility and (2) the relative
52
53 828 permeability of the rock during reaction.
54
55
56
57
58
59
60

1
2
3 829 The length-scale of mass transport (1) or interconnected porosity is important as it
4
5 830 controls the bulk composition of the equilibrium system and thus determines the products of the
6
7
8 831 reaction. This can be demonstrated using Figure 11a as an example. Assuming a rock with bulk
9
10 832 composition X_0 is chemically isolated (i.e. closed system) and equilibrates at 1.2 GPa then the
11
12 833 resulting mineral assemblage will be: hornblende, garnet, plagioclase, clinozoisite, muscovite,
13
14 834 quartz, kyanite, and zoisite. If that rock is, however, connected via a fluid saturated network of
15
16 835 pores with an equivalent mass of rock with bulk composition X_2 then the equilibrium
17
18 836 composition will now be approximately X_1 and the equilibrium assemblage at 1.2 GPa will no
19
20 837 longer contain garnet. This relies on the assumption that element diffusion is primarily facilitated
21
22 838 by the grain boundary fluid and that minerals are in local equilibrium with the grain boundary
23
24 839 fluid. Both are reasonable assumptions given that mineral replacement proceeds as dissolution-
25
26 840 precipitation reaction and that fluid is in excess. Differing length-scales of element mobility can
27
28 841 explain the local occurrence of extreme compositions, inherited from the original compositional
29
30 842 variation of the rock (i.e. where transport length-scales are small; Fig. 13d). Accordingly, at
31
32 843 larger mass transport length-scales, there should be a homogenisation of the compositional
33
34 844 heterogeneity that results from the original mineral distribution. Hence, while fluid connectivity
35
36 845 will facilitate element exchange, a gradient caused by a disparity in either the rates or driving
37
38 846 force of reaction between the compositionally distinct layers is further required for
39
40 847 differentiation.

41
42 848 Here, the interpretation is based on the observation of distinct zones exhibiting (I)
43
44 849 reaction under conditions where permeability, effective normal stress, and dissolution are
45
46 850 decreased vs. (II) reaction under conditions where permeability, effective normal stress, and
47
48 851 dissolution are increased. The inference being that the relative permeability and hence the
49
50
51
52
53
54
55
56
57
58
59
60

1
2
3 852 effective normal stress influences the rate of dissolution. Increased dissolution in areas of
4
5 853 increased effective normal stress is consistent with the proposition that stress enhances
6
7 854 dissolution via increasing the elastic energy through deformation of a grain surface (Den Brok *et*
8
9 855 *al.*, 2002, Den Brok & Morel, 2001, Koehn *et al.*, 2003). Furthermore, it commonly asserted that
10
11 856 increased stress on an interface will result in a relatively increased chemical potential at that
12
13 857 interface (Paterson, 1973, Shimizu, 1995, Wheeler, 2018). Areas of high effective normal stress
14
15 858 will then have a strong chemical potential relative to relatively low stress areas (Rutter, 1983,
16
17 859 Wintsch, 1985). The resulting chemical potential gradient enables mass transport towards low
18
19 860 permeability zones where precipitation will take place. Correlation between high permeability,
20
21 861 stress and enhanced dissolution has been observed and modelled elsewhere for systems
22
23 862 undergoing reaction via dissolution and precipitation (Kelka *et al.*, 2017), producing a
24
25 863 compositionally and texturally banded rock via mass exchange.
26
27
28
29
30

31 864 Enhanced dissolution in localised high-permeability areas coupled with distinct element
32
33 865 solubilities and preferential mobilization of MgO, K₂O, and Fe^{tot} may thus explain the presence
34
35 866 of quartz-enriched and leucocratic domains. Leucocratic domains may then form as zones of
36
37 867 strain-enhanced dissolution (Fig. 13b) around quartz-enriched domains, resulting in the
38
39 868 mobilization of MgO, K₂O, and Fe^{tot} by a dilute NaCl-bearing aqueous fluid (Fig. 13e). The
40
41 869 relative depletion of K₂O, Fe^{tot}, and MgO and minor enrichment of SiO₂, Al₂O₃, Na₂O, and CaO
42
43 870 in the leucocratic domains are consistent with previous experimental work indicating that Si and
44
45 871 Al are far less mobile in Cl-bearing fluids than metals (Shmulovich *et al.*, 2001, Vidale, 1969).
46
47 872 The differences in element mobility can be related to distinct solubilities of Na, Ca, and Mg in
48
49 873 saline fluid due to the formation of fluid-mobile alkali and earth-alkali Cl complexes (Anderson
50
51 874 & Burnham, 1983, Shmulovich *et al.*, 2001). The mass-balance calculation indicates that the
52
53
54
55
56
57
58
59
60

1
2
3 875 mobilized elements were then either transported and precipitated into amphibolite domains of the
4
5 876 shear zone or mobilized from the system, resulting in the slight overall mass loss from the shear
6
7
8 877 zone.

11 878 **CONCLUSIONS**

13
14 879 A common interpretation of quartz-enriched microstructures in amphibolite and eclogite-facies
15
16 880 metamorphic environments is that they form via the precipitation of externally derived elements.
17
18 881 Mass-balance calculations indicate that in this instance the quartz-enrichment observed along
19
20 882 fractures and within the shear zone lithology is indicative of localised mass loss. Localised
21
22 883 depletion of MgO, Fe^{tot} and K₂O around high dissolution seams is due to the increased
23
24 884 compatibility of these elements with the infiltrating Cl-bearing aqueous fluid relative to the
25
26 885 reacting solid. Locally enhanced dissolution thus provides an alternative mechanism for the
27
28 886 localisation of elements in high-pressure environments.

30
31
32 887 Locally enhanced dissolution around fracture pathways ultimately results in the
33
34 888 metamorphic differentiation of the shear zone lithology, and on a larger scale also to the
35
36 889 observed differentiation of elements between the statically hydrated rock and the shear zone
37
38 890 lithologies. The coupling between enhanced dissolution leading to mass loss along high
39
40 891 permeability zones and the relative gain of elements in statically hydrated rocks supports
41
42 892 dissolution-precipitation facilitated mass transfer. Mass transfer is driven by chemical potential
43
44 893 and solubility gradients. Here it is demonstrated that deviations in permeability and hence
45
46 894 effective normal stress may result in the formation of both chemical potential and solubility
47
48 895 gradients.

1
2
3 896 **ACKNOWLEDGEMENTS**
4
5

6 897 This manuscript has been improved by the review of U. Kelka, R. Palin and one anonymous
7
8 898 reviewer. An early version of this manuscript was reviewed by J. Ague and C. Spandler. This
9
10 899 research was funded by the Australian Research Council Discovery Project of Putnis, Raimondo,
11
12 900 and Daczko (ARC grant number DP160103449). The authors acknowledge the facilities, and the
13
14 901 scientific and technical assistance of the Australian Microscopy and Microanalysis Research
15
16 902 Facility at the Centre for Microscopy, Characterisation and Analysis, The University of Western
17
18 903 Australia, a facility funded by the University, State and Commonwealth Governments. Part of
19
20 904 this research was undertaken using the EM instrumentation (ARC LE130100053) at the John de
21
22 905 Laeter Centre, Curtin University.
23
24
25
26

27 906 **DATA AVAILABILITY**
28
29

30 907 The data underlying this article are available in the article and in its online supplementary
31
32 908 material.
33
34
35
36
37
38
39
40
41
42
43
44
45
46
47
48
49
50
51
52
53
54
55
56
57
58
59
60

909 **REFERENCES**

- 910 Ague, J. J. (1994). Mass transfer during Barrovian metamorphism of pelites, south-central
911 Connecticut; I, Evidence for changes in composition and volume. *American Journal of Science*
912 **294**, 989-1057.
- 913 Ague, J. J. & Van Haren, J. L. (1996). Assessing metasomatic mass and volume changes using
914 the bootstrap, with application to deep crustal hydrothermal alteration of marble. *Economic*
915 *geology* **91**, 1169-1182.
- 916 Andersen, T., Austrheim, H. & Burke, E. A. J. (1991). Fluid-induced retrogression of granulites
917 in the Bergen Arcs, Caledonides of W. Norway: Fluid inclusion evidence from amphibolite-
918 facies shear zones. *Lithos* **27**, 29-42.
- 919 Anderson, G. & Burnham, C. W. (1983). Feldspar solubility and the transport of aluminum under
920 metamorphic conditions. *American Journal of Science* **283 A**, 283-297.
- 921 Armstrong, J. (1988). Quantitative analysis of silicate and oxide materials: comparison of monte
922 carlo, ZAF, and ψ (ρz) procedures. *Microbeam analysis*, 239-246.
- 923 Austrheim, H. (1987). Eclogitization of lower crustal granulites by fluid migration through shear
924 zones. *Earth and Planetary Science Letters* **81**, 221-232.
- 925 Austrheim, H. (1990). Fluid induced processes in the lower crust as evidenced by Caledonian
926 eclogitization of Precambrian granulites, Bergen Arcs, western-Norway.
- 927 Beinlich, A., John, T., Vrijmoed, J., Tominaga, M., Magna, T. & Podladchikov, Y. (2020).
928 Instantaneous rock transformations in the deep crust driven by reactive fluid flow. *Nature*
929 *Geoscience* **13**, 307-311.
- 930 Bingen, B., Davis, W. J. & Austrheim, H. (2001). Zircon U-Pb geochronology in the Bergen arc
931 eclogites and their Proterozoic protoliths, and implications for the pre-Scandian evolution of the
932 Caledonides in western Norway. *Geological Society of America Bulletin* **113**, 640-649.

- 1
2
3 933 Bons, P. D. & Jessell, M. W. (1997). Experimental simulation of the formation of fibrous veins
4 934 by localised dissolution-precipitation creep. *Mineralogical magazine* **61**, 53-63.
- 5
6
7
8 935 Boundy, T. M., Essene, E. J., Hall, C. M., Austrheim, H. & Halliday, A. (1996). Rapid
9 936 exhumation of lower crust during continent-continent collision and late extension: Evidence
10 937 from $^{40}\text{Ar}/^{39}\text{Ar}$ incremental heating of hornblendes and muscovites, Caledonian orogen, western
11 938 Norway. *Geological Society of America Bulletin* **108**, 1425-1437.
- 12
13
14
15
16 939 Boundy, T. M., Mezger, K. & Essene, E. J. (1997). Temporal and tectonic evolution of the
17 940 granulite-eclogite association from the Bergen Arcs, western Norway. *Lithos* **39**, 159-178.
- 18
19
20
21 941 Carlson, W. (2010). Dependence of reaction kinetics on H₂O activity as inferred from rates of
22 942 intergranular diffusion of aluminium. *Journal of Metamorphic Geology* **28**, 735-752.
- 23
24
25
26 943 Centrella, S., Austrheim, H. & Putnis, A. (2015). Coupled mass transfer through a fluid phase
27 944 and volume preservation during the hydration of granulite: An example from the Bergen Arcs,
28 945 Norway. *Lithos* **236**, 245-255.
- 29
30
31
32
33 946 Cohen, A., O'Nions, R., Siegenthaler, R. & Griffin, W. (1988). Chronology of the pressure-
34 947 temperature history recorded by a granulite terrain. *Contributions to Mineralogy and Petrology*
35 948 **98**, 303-311.
- 36
37
38
39
40 949 Cox, S. (2010). The application of failure mode diagrams for exploring the roles of fluid pressure
41 950 and stress states in controlling styles of fracture-controlled permeability enhancement in faults
42 951 and shear zones. *Geofluids* **10**, 217-233.
- 43
44
45
46 952 Dahlen, F. (1992). Metamorphism of nonhydrostatically stressed rocks. *American Journal of*
47 953 *Science* **292**, 184-198.
- 48
49
50
51 954 Den Brok, B., Morel, J. & Zahid, M. (2002). In situ experimental study of roughness
52 955 development at a stressed solid/fluid interface. *Geological Society, London, Special Publications*
53 956 **200**, 73-83.
- 54
55
56
57
58
59
60

- 1
2
3 957 Den Brok, S. & Morel, J. (2001). The effect of elastic strain on the microstructure of free
4
5 958 surfaces of stressed minerals in contact with an aqueous solution. *Geophysical Research Letters*
6
7 959 **28**, 603-606.
8
9
10 960 Dewers, T. & Ortoleva, P. (1990). Geochemical self-organization III: A mechano-chemical
11
12 961 model of metamorphic differentiation. *Am. J. Sci* **290**, 473-521.
13
14
15 962 Dipple, G., Wintsch, R. & Andrews, M. (1990). Identification of the scales of differential
16
17 963 element mobility in a ductile fault zone. *Journal of Metamorphic Geology* **8**, 645-661.
18
19
20 964 Dipple, G. M. & Ferry, J. M. (1992). Metasomatism and fluid flow in ductile fault zones.
21
22 965 *Contributions to Mineralogy and Petrology* **112**, 149-164.
23
24
25 966 Donovan, J. J., Snyder, D. A. & Rivers, M. L. (1992). An improved interference correction for
26
27 967 trace element analysis. *Proceedings of the Annual Meeting-Electron Microscopy Society of*
28
29 968 *America*: San francisco press, 1646-1646.
30
31
32 969 Donovan, J. J. & Tingle, T. N. (1996). An improved mean atomic number background correction
33
34 970 for quantitative microanalysis. *Microscopy and Microanalysis* **2**, 1-7.
35
36
37 971 Fisher, G. W. (1970). The application of ionic equilibria to metamorphic differentiation: an
38
39 972 example. *Contributions to Mineralogy and Petrology* **29**, 91-103.
40
41
42 973 Glodny, J., Kühn, A. & Austrheim, H. (2002). Rb/Sr record of fluid-rock interaction in eclogites,
43
44 974 Bergen Arcs, Norway. *Geochimica et cosmochimica acta* **66**, A280-A280.
45
46
47 975 Glodny, J., Kühn, A. & Austrheim, H. (2008). Geochronology of fluid-induced eclogite and
48
49 976 amphibolite facies metamorphic reactions in a subduction–collision system, Bergen Arcs,
50
51 977 Norway. *Contributions to Mineralogy and Petrology* **156**, 27-48.
52
53
54 978 Grant, J. A. (1986). The isocon diagram; a simple solution to Gresens' equation for metasomatic
55
56 979 alteration. *Economic geology* **81**, 1976-1982.
57
58
59
60

- 1
2
3 980 Green, E., White, R., Diener, J., Powell, R., Holland, T. & Palin, R. (2016). Activity–
4 981 composition relations for the calculation of partial melting equilibria in metabasic rocks. *Journal*
5 982 *of Metamorphic Geology* **34**, 845-869.
- 6
7
8
9
10 983 Hawthorne, F. C., Oberti, R., Harlow, G. E., Maresch, W. V., Martin, R. F., Schumacher, J. C. &
11 984 Welch, M. D. (2012). Nomenclature of the amphibole supergroup. *American mineralogist* **97**,
12 985 2031-2048.
- 13
14
15
16 986 Hill, D. P. (2015). On the sensitivity of transtensional versus transpressional tectonic regimes to
17 987 remote dynamic triggering by Coulomb failure. *Bulletin of the Seismological Society of America*
18 988 **105**, 1339-1348.
- 19
20
21
22
23 989 Holland, T. & Powell, R. (2003). Activity–composition relations for phases in petrological
24 990 calculations: an asymmetric multicomponent formulation. *Contributions to Mineralogy and*
25 991 *Petrology* **145**, 492-501.
- 26
27
28
29
30 992 Holland, T. & Powell, R. (2011). An improved and extended internally consistent
31 993 thermodynamic dataset for phases of petrological interest, involving a new equation of state for
32 994 solids. *Journal of Metamorphic Geology* **29**, 333-383.
- 33
34
35
36 995 Joesten, R. (1977). Evolution of mineral assemblage zoning in diffusion metasomatism.
37 996 *Geochimica et cosmochimica acta* **41**, 649-670.
- 38
39
40
41 997 Kelka, U., Veveakis, M., Koehn, D. & Beaudoin, N. (2017). Zebra rocks: compaction waves
42 998 create ore deposits. *Scientific Reports* **7**, 1-9.
- 43
44
45
46 999 Koehn, D., Arnold, J., Jamtveit, B. & Malthe-Sørensen, A. (2003). Instabilities in stress
47 1000 corrosion and the transition to brittle failure. *American Journal of Science* **303**, 956-971.
- 48
49
50
51 1001 Kullerud, K. (1996). Chlorine-rich amphiboles; interplay between amphibole composition and an
52 1002 evolving fluid. *European Journal of Mineralogy* **8**, 355-370.
- 53
54
55
56
57
58
59
60

- 1
2
3 1003 Lamadrid, H. M., Rimstidt, J. D., Schwarzenbach, E. M., Klein, F., Ulrich, S., Dolocan, A. &
4 1004 Bodnar, R. J. (2017). Effect of water activity on rates of serpentinization of olivine. *Nature*
5 1005 *communications* **8**, 16107.
6
7
8
9
10 1006 Locock, A. J. (2014). An Excel spreadsheet to classify chemical analyses of amphiboles
11 1007 following the IMA 2012 recommendations. *Computers & Geosciences* **62**, 1-11.
12
13
14
15 1008 Markl, G. & Bucher, K. (1998). Composition of fluids in the lower crust inferred from
16 1009 metamorphic salt in lower crustal rocks. *Nature* **391**, 781-783.
17
18
19
20 1010 Markl, G., Ferry, J. & Bucher, K. (1998). Formation of saline brines and salt in the lower crust
21 1011 by hydration reactions in partially retrogressed granulites from the Lofoten Islands, Norway.
22 1012 *American Journal of Science* **298**, 705-757.
23
24
25
26 1013 McDonough, W. F. & Sun, S.-S. (1995). The composition of the Earth. *Chemical geology* **120**,
27 1014 223-253.
28
29
30
31 1015 Moore, J., Beinlich, A., Porter, J. K., Talavera, C., Berndt, J., Piazzolo, S., Austrheim, H. &
32 1016 Putnis, A. (2020). Microstructurally controlled trace element (Zr, U–Pb) concentrations in
33 1017 metamorphic rutile: An example from the amphibolites of the Bergen Arcs. *Journal of*
34 1018 *Metamorphic Geology* **38**, 103-127.
35
36
37
38
39
40 1019 Moore, J., Beinlich, A., Putnis, A. & Austrheim, H. (2019). Stress orientation–dependent
41 1020 reactions during metamorphism. *Geology* **47**, 151-154.
42
43
44
45 1021 Oelkers, E. H. & Helgeson, H. C. (1988). Calculation of the thermodynamic and transport
46 1022 properties of aqueous species at high pressures and temperatures: Aqueous tracer diffusion
47 1023 coefficients of ions to 1000°C and 5 kb. *Geochimica et cosmochimica acta* **52**, 63-85.
48
49
50
51 1024 Orville, P. M. (1969). A model for metamorphic differentiation origin of thin-layered
52 1025 amphibolites. *American Journal of Science* **267**, 64-86.
53
54
55
56
57
58
59
60

- 1
2
3 1026 Paterson, M. (1973). Nonhydrostatic thermodynamics and its geologic applications. *Reviews of*
4 1027 *Geophysics* **11**, 355-389.
5
6
7
8 1028 Pattison, D. R. M. (1994). Are reversed Fe-Mg exchange and solid solution experiments really
9 1029 reversed? *American mineralogist* **79**, 938-950.
10
11
12
13 1030 Porter, J. K. & Austrheim, H. (2017). Sulphide formation from granulite-facies S-rich scapolite
14 1031 breakdown. *Terra Nova* **29**, 29-35.
15
16
17
18 1032 Powell, R. & Holland, T. (1988). An internally consistent dataset with uncertainties and
19 1033 correlations: 3. Applications to geobarometry, worked examples and a computer program.
20 1034 *Journal of Metamorphic Geology* **6**, 173-204.
21
22
23
24 1035 Putnis, A. (2009). Mineral replacement reactions. *Reviews in mineralogy and geochemistry* **70**,
26 1036 87-124.
27
28
29 1037 Putnis, A. & Austrheim, H. (2013). Mechanisms of metasomatism and metamorphism on the
30 1038 local mineral scale: the role of dissolution-precipitation during mineral re-equilibration.
31 1039 *Metasomatism and the Chemical Transformation of Rock*: Springer, 141-170.
32
33
34
35
36 1040 Rasband, W. S. (1997-2014). ImageJ. U. S. National Institutes of Health, Bethesda, MD.
37 1041 Available at <http://imagej.nih.gov/ij/>.
38
39
40
41 1042 Rubie, D. C. (1986). The catalysis of mineral reactions by water and restrictions on the presence
42 1043 of aqueous fluid during metamorphism. *Mineralogical magazine* **50**, 399-415.
43
44
45
46 1044 Rutter, E. (1983). Pressure solution in nature, theory and experiment. *Journal of the Geological*
47 1045 *Society* **140**, 725-740.
48
49
50
51 1046 Selverstone, J., Morteani, G. & Staude, J. M. (1991). Fluid channelling during ductile shearing:
52 1047 transformation of granodiorite into aluminous schist in the Tauern Window, Eastern Alps.
53 1048 *Journal of Metamorphic Geology* **9**, 419-431.
54
55
56
57
58
59
60

- 1
2
3 1049 Shimizu, I. (1995). Kinetics of pressure solution creep in quartz: theoretical considerations.
4
5 1050 *Tectonophysics* **245**, 121-134.
6
7
8 1051 Shmulovich, K., Graham, C. & Yardley, B. (2001). Quartz, albite and diopside solubilities in
9
10 1052 H₂O–NaCl and H₂O–CO₂ fluids at 0.5–0.9 GPa. *Contributions to Mineralogy and Petrology* **141**,
11
12 1053 95-108.
13
14
15 1054 Vernon, R. (1979). Formation of late sillimanite by hydrogen metasomatism (base-leaching) in
16
17 1055 some high-grade gneisses. *Lithos* **12**, 143-152.
18
19
20 1056 Vernon, R. (1998). Chemical and volume changes during deformation and prograde
21
22 1057 metamorphism of sediments. *Geological Society, London, Special Publications* **138**, 215-246.
23
24
25 1058 Vernon, R. H. (2018). *A practical guide to rock microstructure*: Cambridge University Press.
26
27
28 1059 Vidale, R. (1969). Metasomatism in a chemical gradient and the formation of calc-silicate bands.
29
30 1060 *American Journal of Science* **267**, 857-874.
31
32
33 1061 Wassmann, S. & Stöckhert, B. (2013). Low stress deformation of garnet by incongruent
34
35 1062 dissolution precipitation creep. *Journal of Structural Geology* **46**, 200-219.
36
37
38 1063 Wheeler, J. (2014). Dramatic effects of stress on metamorphic reactions. *Geology* **42**, 647-650.
39
40
41 1064 Wheeler, J. (2018). The effects of stress on reactions in the Earth: Sometimes rather mean,
42
43 1065 usually normal, always important. *Journal of Metamorphic Geology* **36**, 439-461.
44
45
46 1066 White, R., Powell, R., Holland, T., Johnson, T. & Green, E. (2014). New mineral activity–
47
48 1067 composition relations for thermodynamic calculations in metapelitic systems. *Journal of*
49
50 1068 *Metamorphic Geology* **32**, 261-286.
51
52
53 1069 Whitney, D. L. & Evans, B. W. (2010). Abbreviations for names of rock-forming minerals.
54
55 1070 *American mineralogist* **95**, 185-187.
56
57
58
59
60

- 1
2
3 1071 Williams, P. (1972). Development of metamorphic layering and cleavage in low grade
4 1072 metamorphic rocks at Bermagui, Australia. *American Journal of Science* **272**, 1-47.
5
6
7
8 1073 Williams, P. F. (1990). Differentiated layering in metamorphic rocks. *Earth-Science Reviews* **29**,
9 1074 267-281.
10
11
12
13 1075 Wintsch, R. (1985). The possible effects of deformation on chemical processes in metamorphic
14 1076 fault zones. *Metamorphic reactions*: Springer, 251-268.
15
16
17
18 1077 Wintsch, R., Kvale, C. & Kisch, H. (1991). Open-system, constant-volume development of slaty
19 1078 cleavage, and strain-induced replacement reactions in the Martinsburg Formation, Lehigh Gap,
20 1079 Pennsylvania. *Geological Society of America Bulletin* **103**, 916-927.
21
22
23
24 1080 Wintsch, R. P. & Andrews, M. S. (1988). Deformation induced growth of sillimanite: " Stress"
25 1081 minerals revisited. *The Journal of Geology* **96**, 143-161.
26
27
28
29 1082 Xia, F., Brugger, J., Chen, G., Ngothai, Y., O'Neill, B., Putnis, A. & Pring, A. (2009).
30 1083 Mechanism and kinetics of pseudomorphic mineral replacement reactions: A case study of the
31 1084 replacement of pentlandite by violarite. *Geochimica et cosmochimica acta* **73**, 1945-1969.
32
33
34
35
36 1085 Yund, R. A. (1997). Rates of grain boundary diffusion through enstatite and forsterite reaction
37 1086 rims. *Contributions to Mineralogy and Petrology* **126**, 224-236.
38
39
40

41 **FIGURE CAPTIONS**

- 42
43 1088 Figure 1. Regional setting and outcrop. (a) Study area at Radøy in the Lindås nappe of the
44 1089 Bergen Arcs, Western Norway. Outcrop locality is indicated by yellow star. Locality of
45 1090 amphibolite-facies shear zone of ¹Andersen *et al.* (1991) is indicated by white circle and
46 1091 scapolite veins of ²Porter and Austrheim (2017) are indicated by red circles. MCTZ = Main
47 1092 Caledonian Thrust Zone. BASZ = Bergen Arcs Shear Zone. Modified from Boundy *et al.* (1997),
48 1093 Glodny *et al.* (2008) and Centrella *et al.* (2015). (b) Field relationships between lithologies at
49
50
51
52
53
54
55
56
57
58
59
60

1
2
3 1094 Fjellsende (c) granulite to statically hydrated amphibolite interface, the continuation of the
4
5 1095 granulite foliation into the amphibolite is indicated by the dashed line (S). (d) Fracture and
6
7
8 1096 alteration halo in granulite. (e) Shear zone lithology showing a spaced foliation defined by
9
10 1097 interlayering of amphibolite and leucocratic domains.

11
12
13 1098 Figure 2. TIMA-X Mineral maps for all lithologies: (a) Granulite, (b) fracture in granulite with
14
15 1099 detail of fracture assemblage inset (i). (c) Altered granulite, (d) Amphibolite (e) strained
16
17 1100 amphibolite exhibiting a quartz domain and four additional mineralogical domains (i-iv; for
18
19
20 1101 details see text), and the shear zone lithologies: (f) amphibolite domain (g) leucocratic domain
21
22 1102 exhibiting quartz stringers (i) with rare amphibole (ii), and, (h) quartz-enriched domain within a
23
24 1103 leucocratic domain.

25
26
27 1104 Figure 3. Modal abundance of minerals in the separate lithologies across the granulite-shear zone
28
29 1105 interface. For each of the lithologies modal abundances are calculated as mass percentages based
30
31 1106 on representative TIMA-X maps. Spacing along the x-axis is representative of the distribution of
32
33
34 1107 the lithologies across the outcrop. Mineral abbreviations follow Whitney and Evans 2010.

35
36
37 1108 Figure 4. Backscattered electron (BSE) images of representative assemblages at the granulite-
38
39 1109 amphibolite interface (a, b) and the replacement and breakdown of amphibole in the shear zone
40
41 1110 lithologies (c, d). (a, b) Grain boundary replacement of granulitic diopside, garnet, and
42
43 1111 plagioclase at by amphibolite assemblage. (c) Near-complete replacement of granulite-facies
44
45 1112 minerals in amphibolite. Replacement resulting in amphibolite-facies mineral distributions that
46
47 1113 are reflective of the precursor mineral. (d) Amphibole cluster in the shear zone amphibolite. (e)
48
49 1114 Elongate amphibole in the leucocratic domains.

50
51
52
53 1115 Figure 5. BSE images (a, c-e) and photomicrograph of quartz-lined fractures and a quartz-
54
55 1116 enriched areas hosted in the main lithologies. (a) A quartz-lined fracture intersecting plagioclase

1
2
3 1117 in the granulite. The fracture itself predominantly hosts quartz, oligoclase, bytownite and biotite.
4
5 1118 The alteration halo is comprised of large subhedral-euhedral zoisite, bytownite, andesine, quartz
6
7
8 1119 and minor amounts of kyanite and muscovite. (b) Microstructure of quartz aggregates within
9
10 1120 fracture (c) Quartz-filled fracture intersecting plagioclase in an altered granulite. Here the quartz
11
12 1121 on the fracture plane is accompanied by C-bearing scapolite and tschermakite (d) Foliation
13
14 1122 parallel quartz-enriched area in the strained amphibolite, comprised of quartz, muscovite, biotite
15
16 1123 and andesine. In the rock immediately adjacent to the fracture the size and abundance of zoisite
17
18 1124 and clinozoisite is increased, as reflected in the modal abundance of the rock (Fig. 3.3). (e)
19
20 1125 Quartz-enriched area within a leucocratic domain.
21
22
23

24 1126 Figure 6. Amphibole compositions across the granulite-shear zone transition. All amphiboles
25
26 1127 belong to the amphibolite alteration event. (a) Ca-amphibole classification plot with Cl apfu
27
28 1128 contouring. (b) X_{Mg} versus Cl apfu with the range of concentrations indicated for each of the
29
30 1129 lithologies.
31
32
33

34 1130 Figure 7. Scapolite composition (a) S apfu and (b) Cl apfu in scapolite A-site plotted against
35
36 1131 equivalent anorthite component. (c) Photomicrograph of S-bearing scapolite vein in an altered
37
38 1132 granulite. BSE images of: (d) recrystallisation at S-bearing scapolite grain boundaries, producing
39
40 1133 S-poor scapolite and pyrite. (e) C-rich scapolite aggregate in the amphibolite (f) scapolite in the
41
42 1134 amphibolite domains of the shear zone.
43
44
45

46 1135 Figure 8. Bulk chemistry mass change of major and volatile elements (wt%) in the amphibolite-
47
48 1136 facies lithologies relative to the anorthositic granulite. In all lithologies plagioclase forming
49
50 1137 elements (SiO_2 , Al_2O_3 , Na_2O , and CaO) are highlighted.
51
52

53 1138 Figure 9. Comparison granulite and amphibolite-facies whole rock REE patterns.
54
55
56
57
58
59
60

1
2
3 1139 Figure 10. Thermodynamic modelling of amphibolite mineral assemblages in (a-c) T–X_{H₂O} and
4
5 1140 (d) P–T pseudosections. For each of the T–X_{H₂O} pseudosections zoisite modal isopleths are
6
7 1141 indicated within the assemblage stability fields. (a) The amphibolite mineral assemblage, with
8
9 1142 zoisite at 3 modal %, is stable when bulk H₂O content is increased from the measured amount
10
11 1143 (X₀: 0.26 wt%) to 0.77-0.85 wt%. (b) The amphibolite domain mineral assemblage, with zoisite
12
13 1144 at 3 modal %, is stable when bulk H₂O content is increased from the measured amount (X₀: 0.36
14
15 1145 wt%) to 0.95-1.10 wt%. (b) The leucocratic domain mineral assemblage, with zoisite at 6 modal
16
17 1146 %, is stable at the measured H₂O content (X₀: 0.48 wt%). (d) Amphibolite, amphibolite domain
18
19 1147 and leucocratic domain assemblages modelled in P–T space with the equilibrium H₂O content as
20
21 1148 indicated by T–X_{H₂O} diagrams. Mineral stability fields (i, ii) for the amphibolite assemblages and
22
23 1149 (iii) for the leucocratic domains, are consistent with the results of individual
24
25 1150 geothermobarometers (for details see; Moore *et al.*, 2020).

26
27
28
29
30
31 1151 Figure 11. Thermodynamic modelling of mass transfer and assemblage distribution in the shear
32
33 1152 zone rock. (a) P–X pseudosection of the shear zone rock lithologies at the thermodynamically
34
35 1153 estimated H₂O composition. Beneath the pseudosection is the mass change comparison of the
36
37 1154 leucocratic domains and amphibolite domains within the shear zone rock and the entire shear
38
39 1155 zone rock in comparison to the granulite. (b) Calculated mineral mass percentages at the
40
41 1156 observed zoisite abundances each composition. (c) Observed mineral mass percentages in the
42
43 1157 shear zone lithologies.

44
45
46
47 1158 Figure 12. Comparison of the calculated partial melt mass changes (a, b) with the measured mass
48
49 1159 change in the shear zone lithologies (c, d). All mass gains and losses are relative to the
50
51 1160 anhydrous granulite.

1
2
3 1161 Figure 13. Conceptual model for the characteristic elemental and textural distributions associated
4
5 1162 with the amphibolite facies hydration and deformation event. (a) Initial fluid infiltrates granulite
6
7 1163 along pre-existing fractures of varying size. Fractures are illustrated as concentrated damage
8
9 1164 zones, the damage to the rock progressively decreasing outwards from the central fracture,
10
11 1165 providing pathways for the percolation of fluid outwards from fractures. The stages illustrated in
12
13 1166 (b) and (c) are simultaneous. (b) Illustration of the initial stress distribution that results from the
14
15 1167 fracturing. The concentration of stress on a central plane enhances both fluid availability and
16
17 1168 dissolution within that zone (c) Due to the heterogeneous strain and fluid distribution the
18
19 1169 minerals grown in each domain have different characteristic textures. Minerals grown in the
20
21 1170 central fracture - quartz-enriched domains- have a microstructure characteristic of crystal growth
22
23 1171 in a free fluid. Minerals grown in the outer fracture damage zones - the amphibolite - are
24
25 1172 characteristic of interface-coupled dissolution and precipitation, leading to pseudomorphic
26
27 1173 replacement of granulite facies minerals. In areas where fracture zones are relatively small (I)
28
29 1174 then deformation is not induced and fluid connectivity is reduced, resulting in continued reaction
30
31 1175 within a system that is closed at the mm to cm scale, as shown in (d). Here H₂O consuming
32
33 1176 reactions leave a final fluid that is concentrated in Cl, precipitating Cl-enriched minerals along
34
35 1177 fractures. In areas where fracture damage zones are sufficiently large (II) and the localisation of
36
37 1178 shear is facilitated as shown in (e) then deformation enables continued fluid connectivity on at
38
39 1179 least the cm-dm scale. The combined continued fluid connectivity and deformation results in a
40
41 1180 system that is open at this larger scale. Continued connectivity results in the leaching of elements
42
43 1181 (Mg, Fe, and K) from the leucocratic domains, transporting them into the amphibolite domains.
44
45
46
47
48
49
50
51
52
53
54
55
56
57
58
59
60

Figure 1

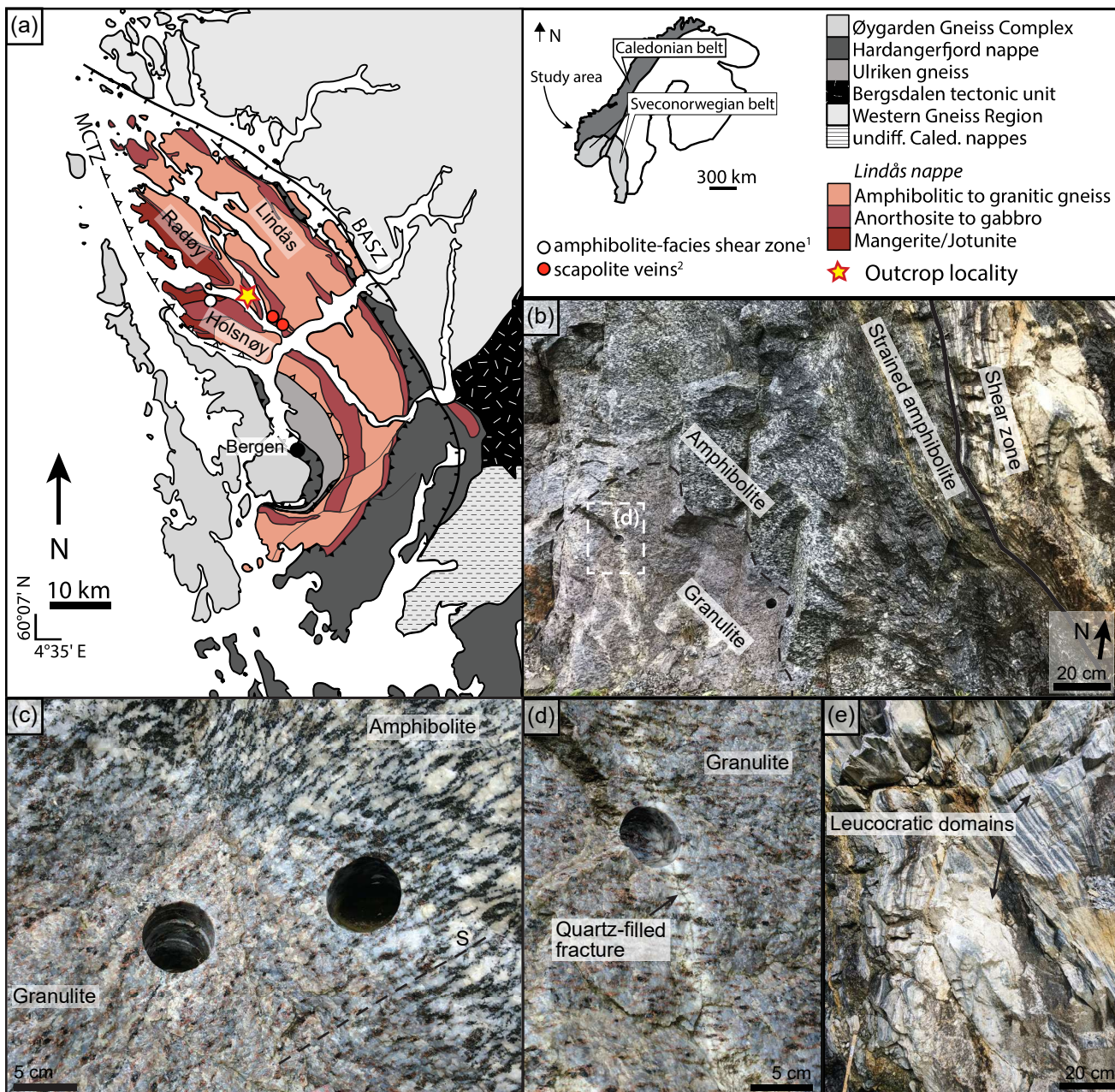
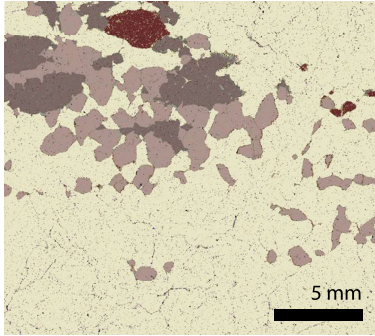
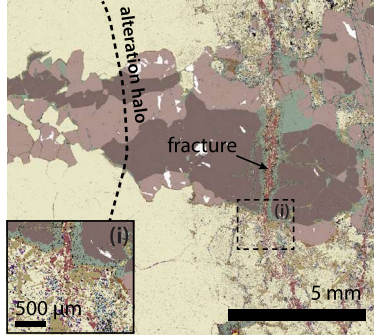


Figure 2

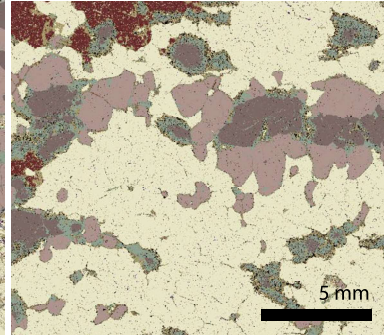
(a) Granulite



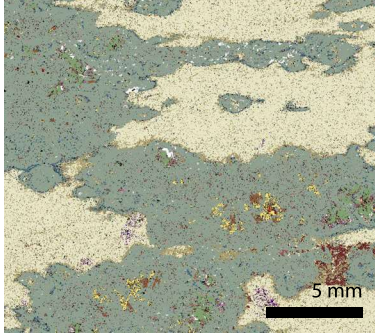
(b) Quartz-filled fracture



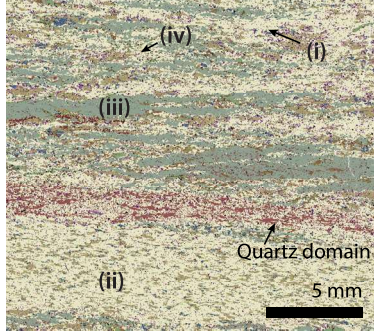
(c) Altered granulite

















(d) Amphibolite



(e) Strained amphibolite

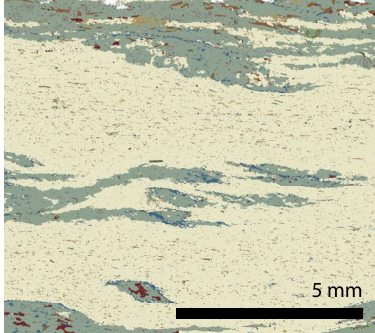


Phases

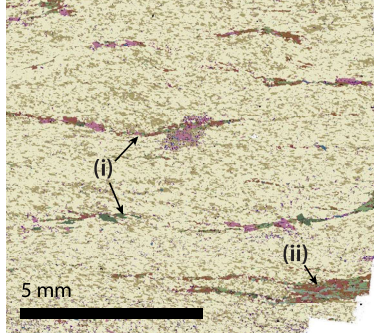
 Plagioclase	 Scapolite
 Garnet	 Biotite
 Diopside	 Chlorite
 Amphibole	 White mica
 Zoisite	 Clinzoisite
 Kyanite	 Carbonate
 Quartz	 Rutile

SHEAR ZONE

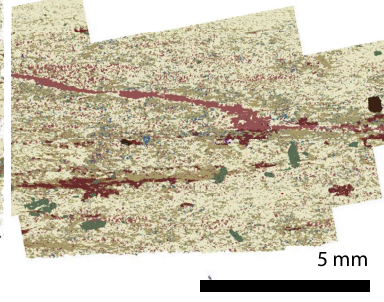
(f) Amphibolite domain



(g) Leucocratic domain



(h) Quartz domain (occurring within leucocratic domains)



2
3
4
5
6
7
8
9
10
11
12
13
14
15
16
17
18
19
20
21
22
23
24
25
26
27
28
29
30
31
32
33
34
35
36
37
38
39
40
41
42
43
44
45
46
47
48
49
50
51
52
53
54
55
56
57
58
59
60

Figure 3

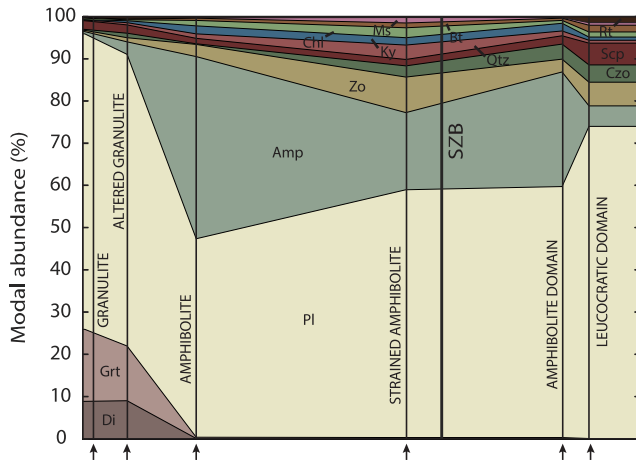


Figure 4

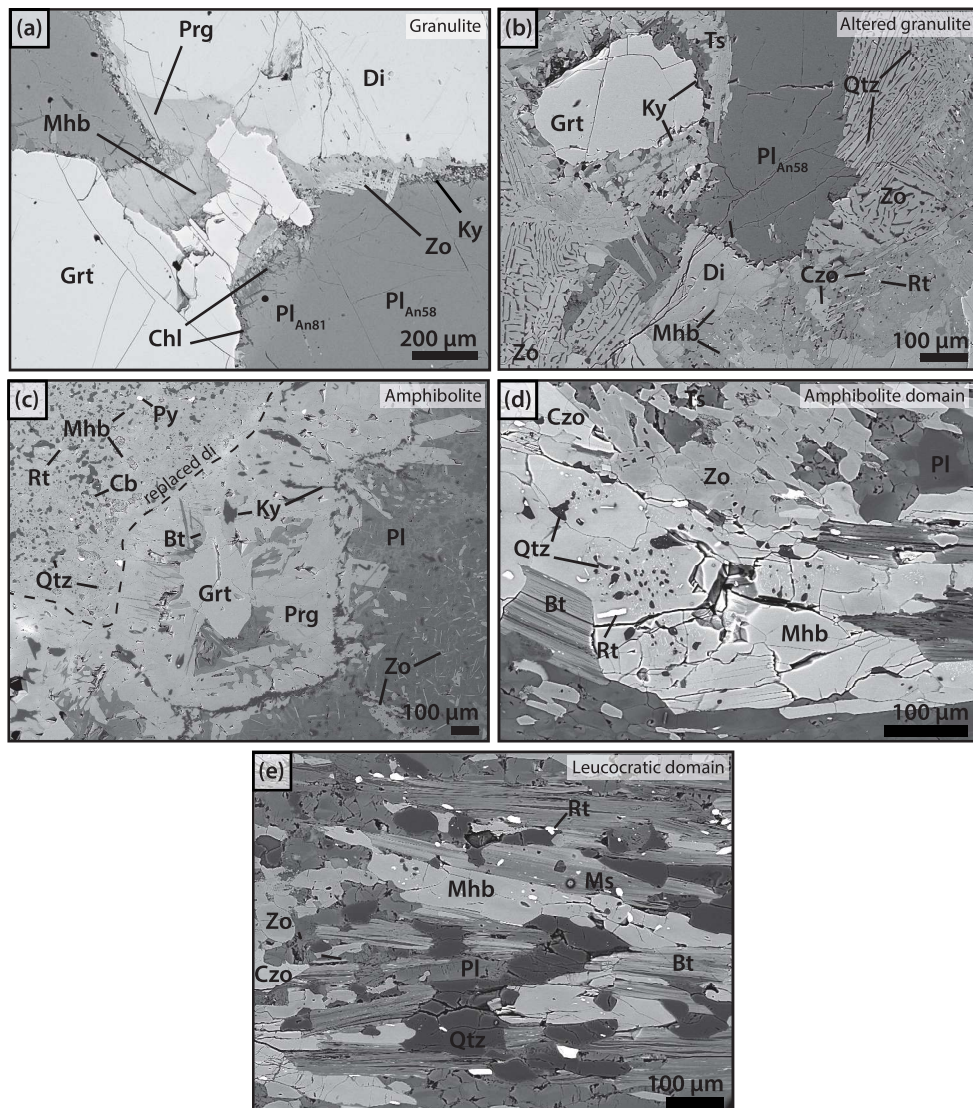


Figure 5

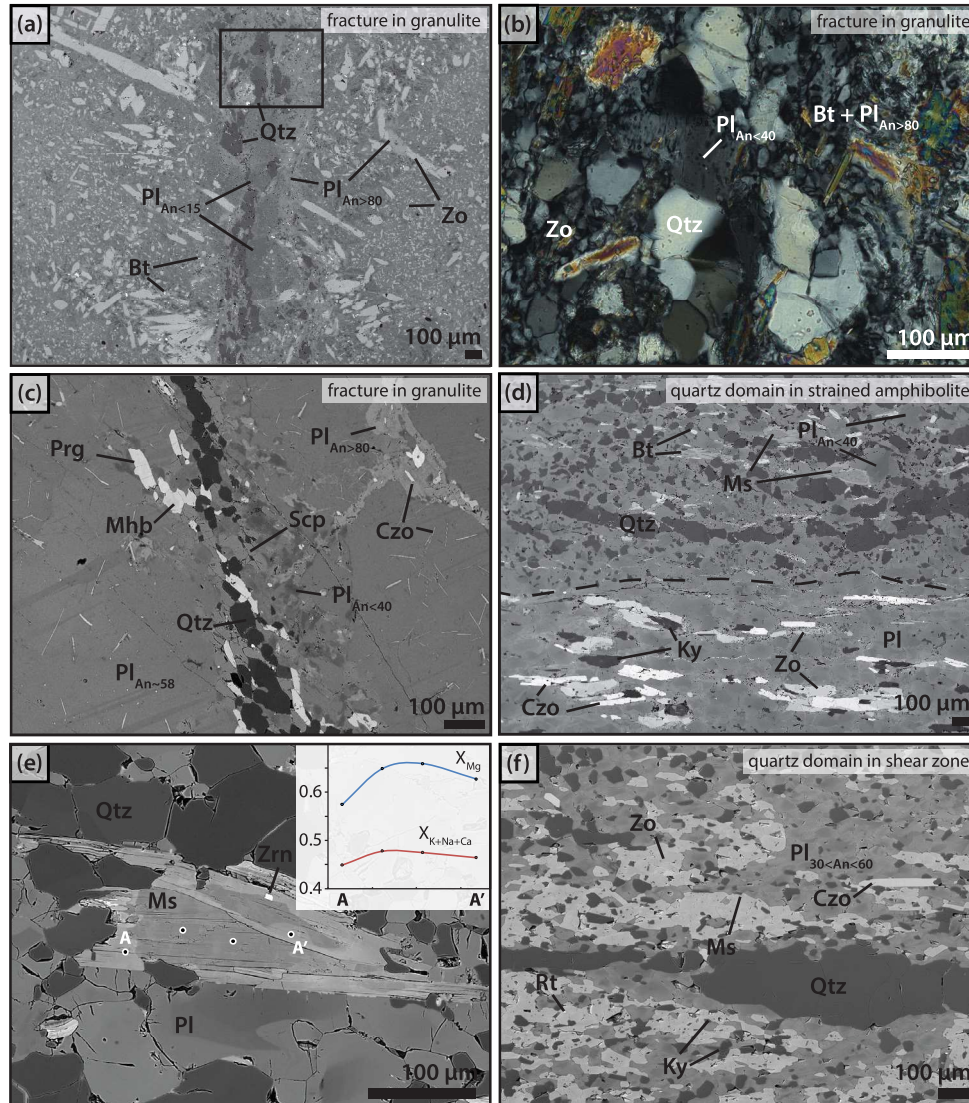


Figure 6

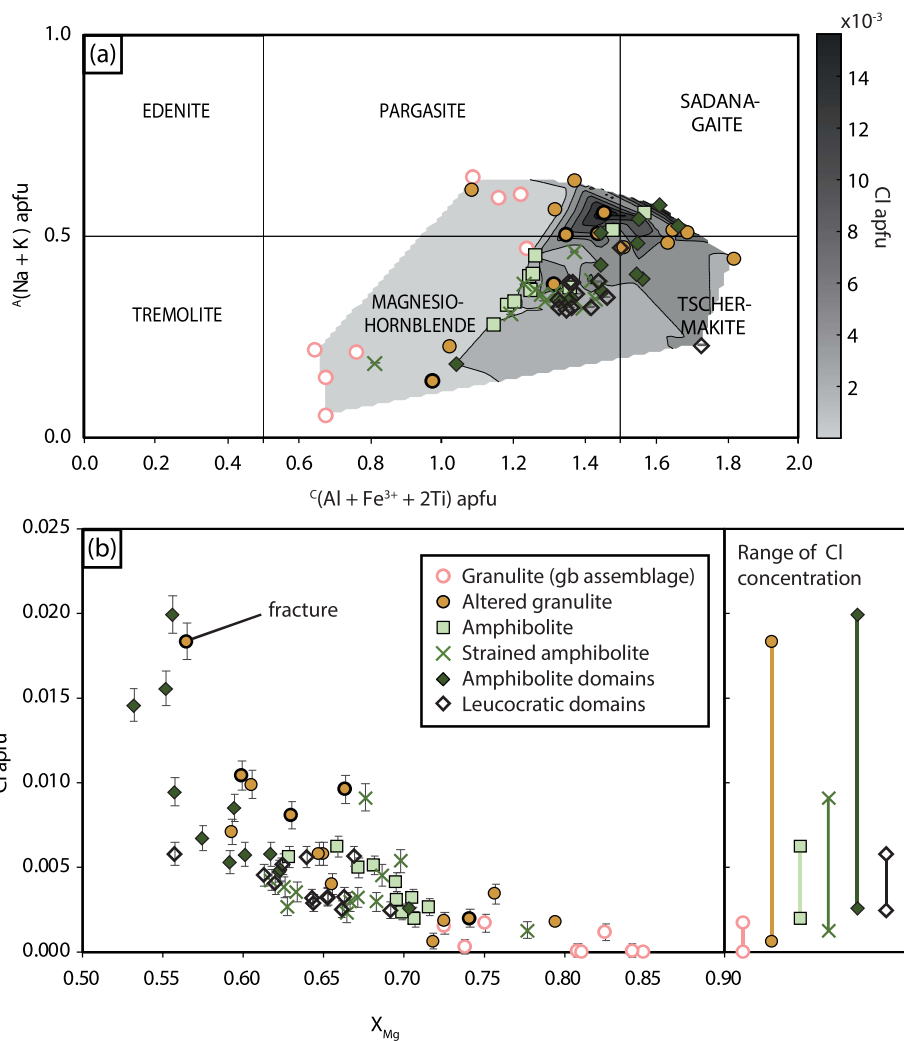


Figure 7

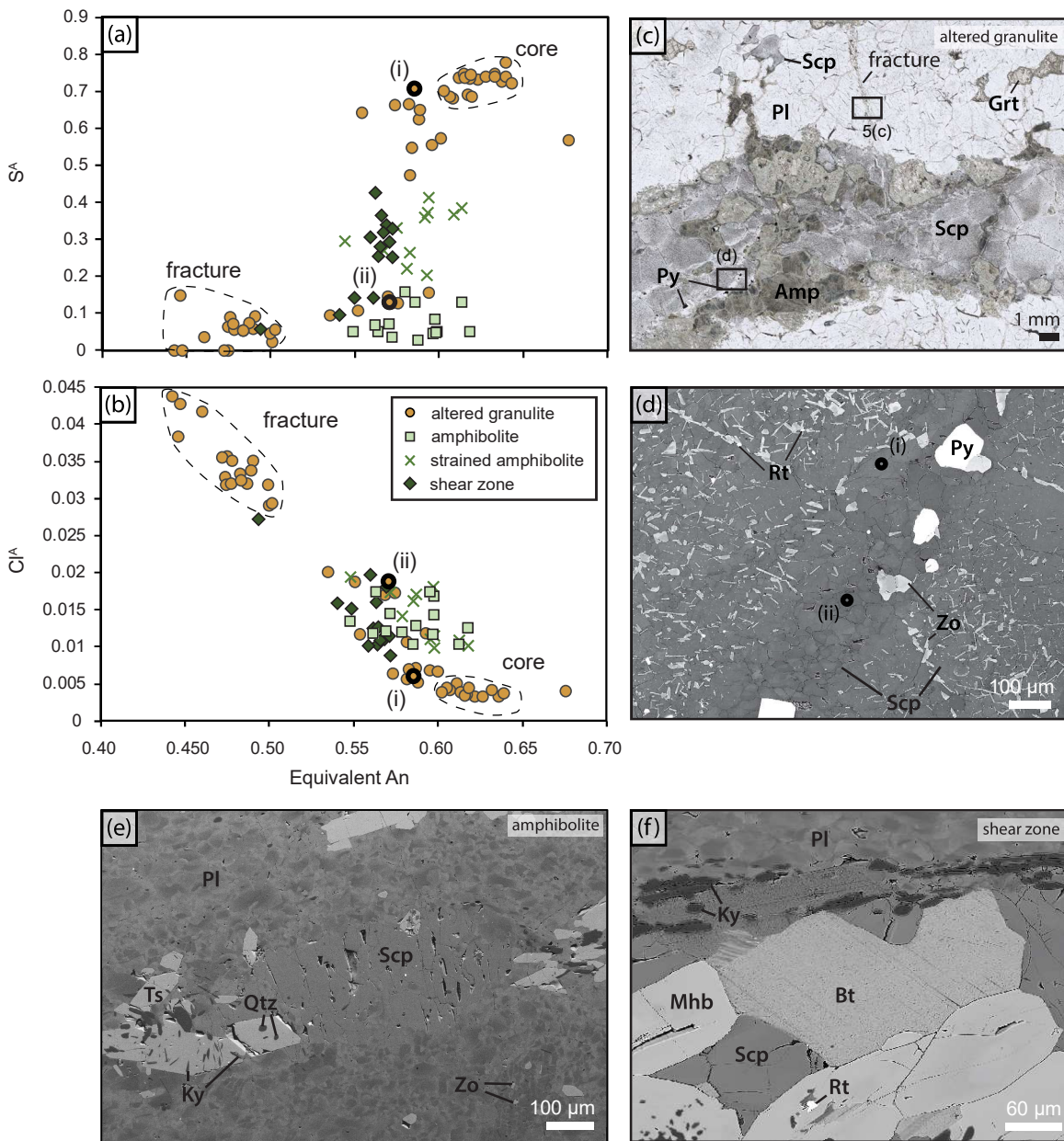


Figure 8

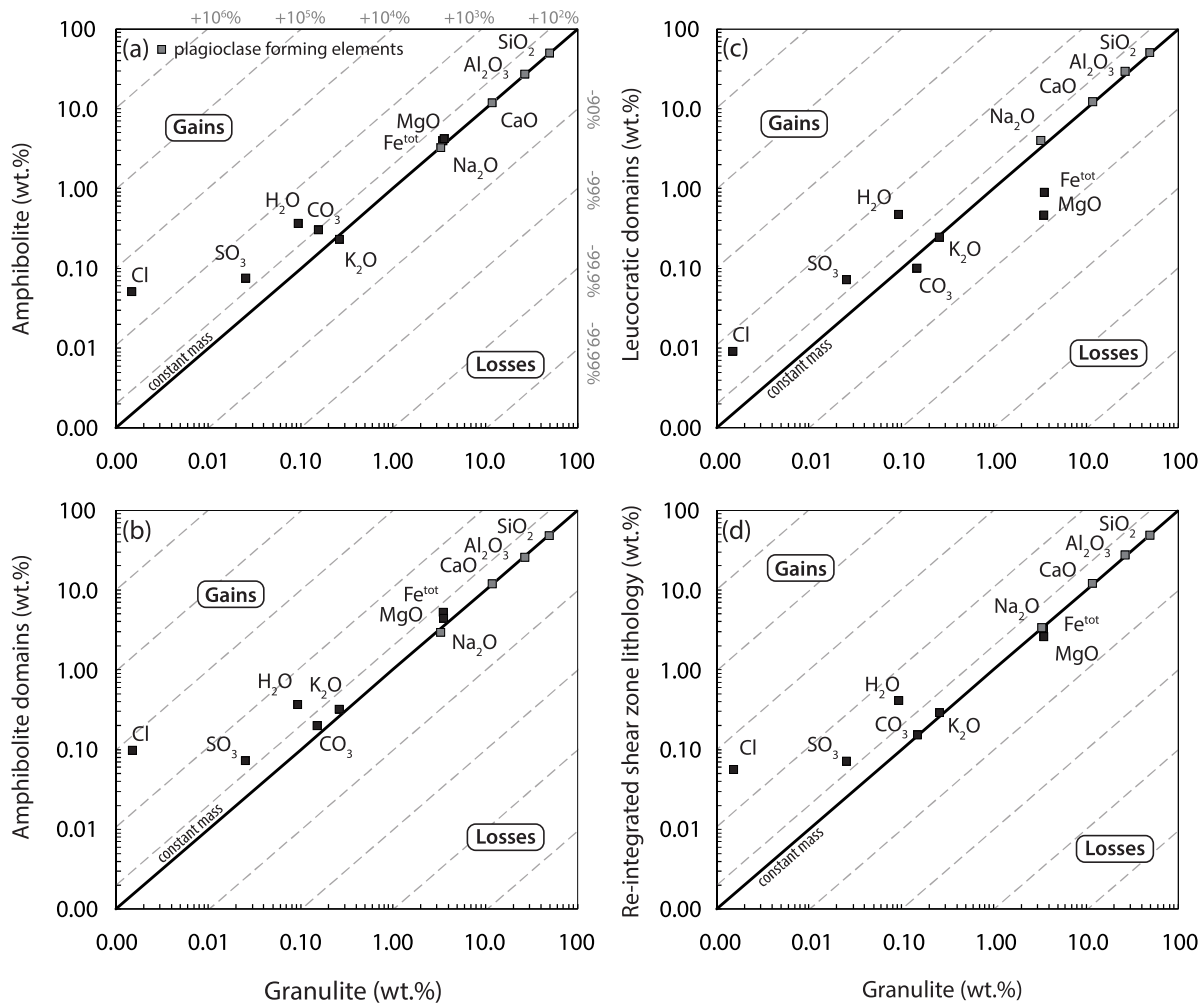


Figure 9

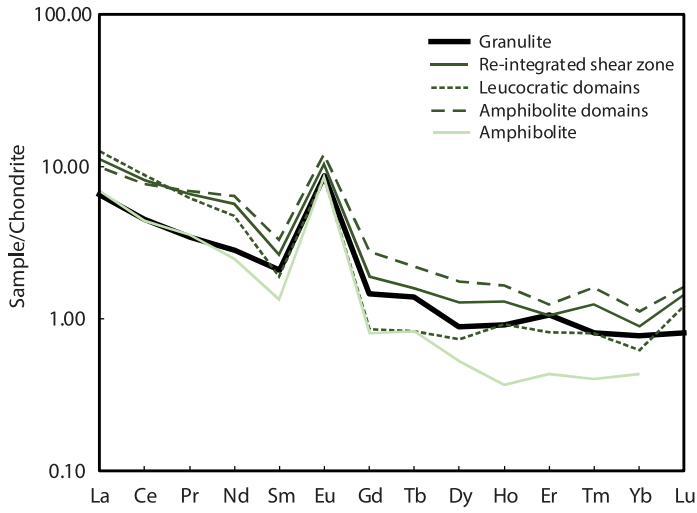


Figure 10

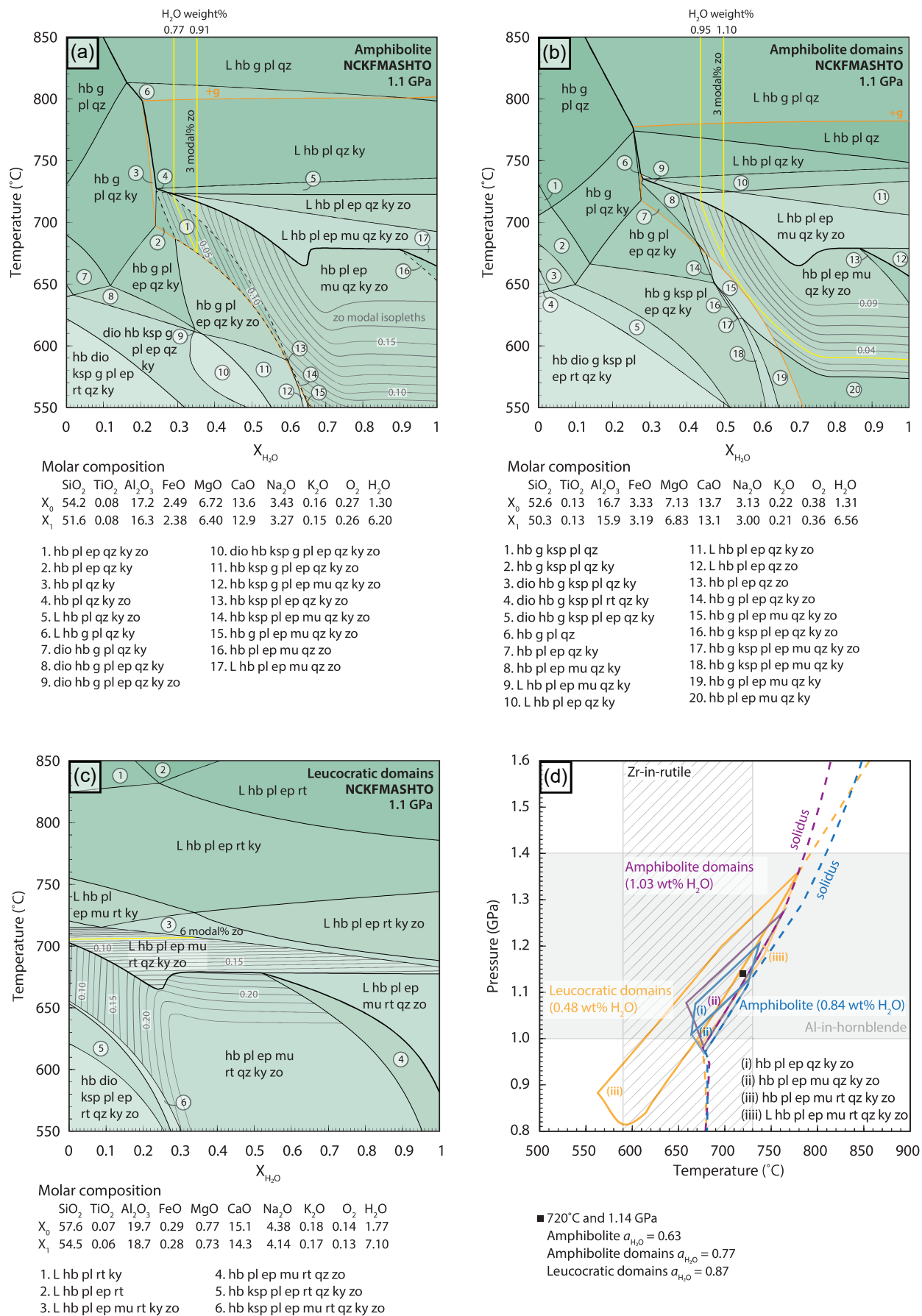
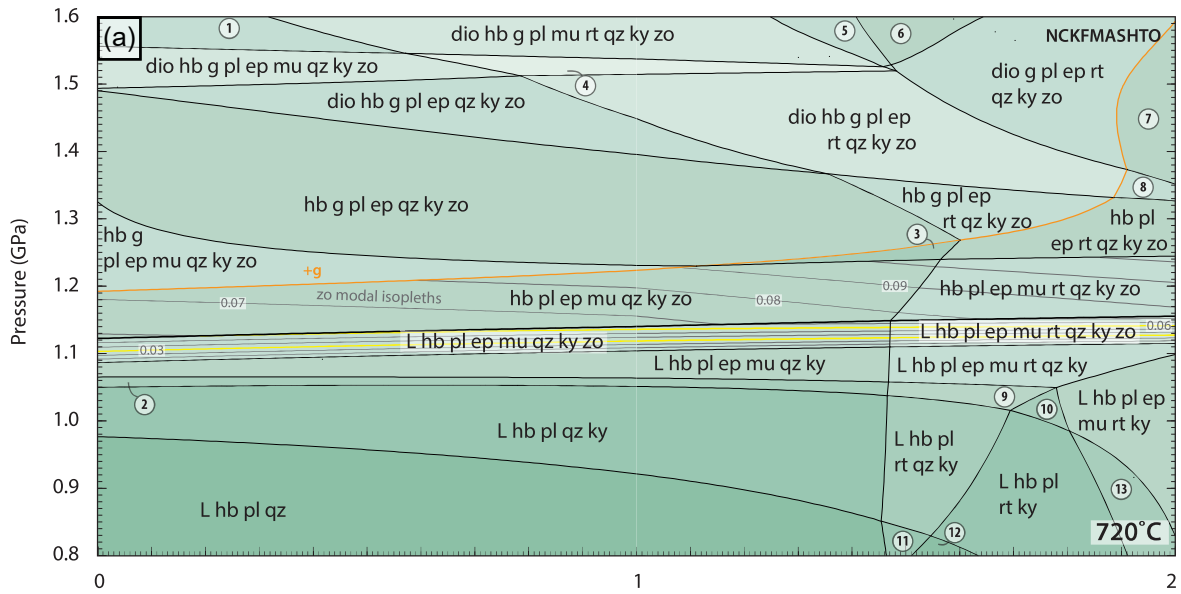


Figure 11



Molar composition

	SiO ₂	TiO ₂	Al ₂ O ₃	FeO	MgO	CaO	Na ₂ O	K ₂ O	O ₂	H ₂ O
X ₀	52.0	0.13	16.5	3.30	7.06	13.6	3.10	0.22	0.37	3.80
X ₁	54.4	0.10	17.9	1.94	4.22	14.2	3.66	0.20	0.27	2.87
X ₂	56.1	0.07	19.6	0.29	0.77	15.0	4.35	0.18	0.14	1.77

- | | |
|----------------------------------|-----------------------------|
| 1. dio hb g pl mu qz ky zo | 8. dio hb pl ep rt qz ky zo |
| 2. L hb pl ep qz ky | 9. L hb pl ep rt qz ky |
| 3. hb pl ep qz ky zo | 10. L hb pl ep rt ky |
| 4. dio hb g pl mu ep rt qz ky zo | 11. L hb pl rt qz |
| 5. dio g pl mu ep rt qz ky zo | 12. L hb pl rt |
| 6. dio hb g pl rt qz ky zo | 13. L hb pl mu rt ky |
| 7. dio pl ep rt qz ky zo | |

Amphibolite domains (X₀)

- 3% SiO₂
- 14% Na₂O
- 6% Al₂O₃
- 3% CaO
- + 11% K₂O
- + 33% H₂O
- + 71% Cl
- + 62% Fe₂O₃
- + 70% MgO

Relative to shear zone rock

Re-integrated shear zone rock (X₁)

- 1% SiO₂
- + 5% Na₂O
- + 2% Al₂O₃
- + 1% CaO
- + 9% K₂O
- + 760% H₂O
- + 3600% Cl
- 7% Fe₂O₃
- 27% MgO

Relative to granulite

Leucocratic domains (X₂)

- + 3% SiO₂
- + 16% Na₂O
- + 7% Al₂O₃
- + 3% CaO
- 13% K₂O
- 38% H₂O
- 84% Cl
- 73% Fe₂O₃
- 82% MgO

Relative to shear zone rock

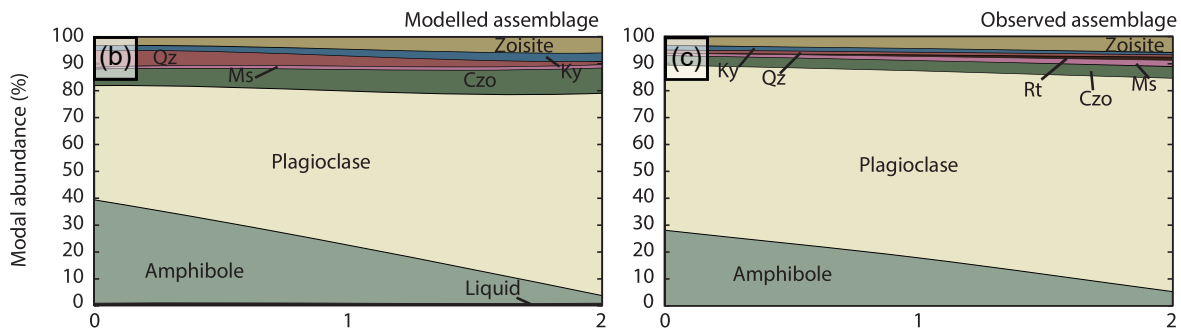


Figure 12

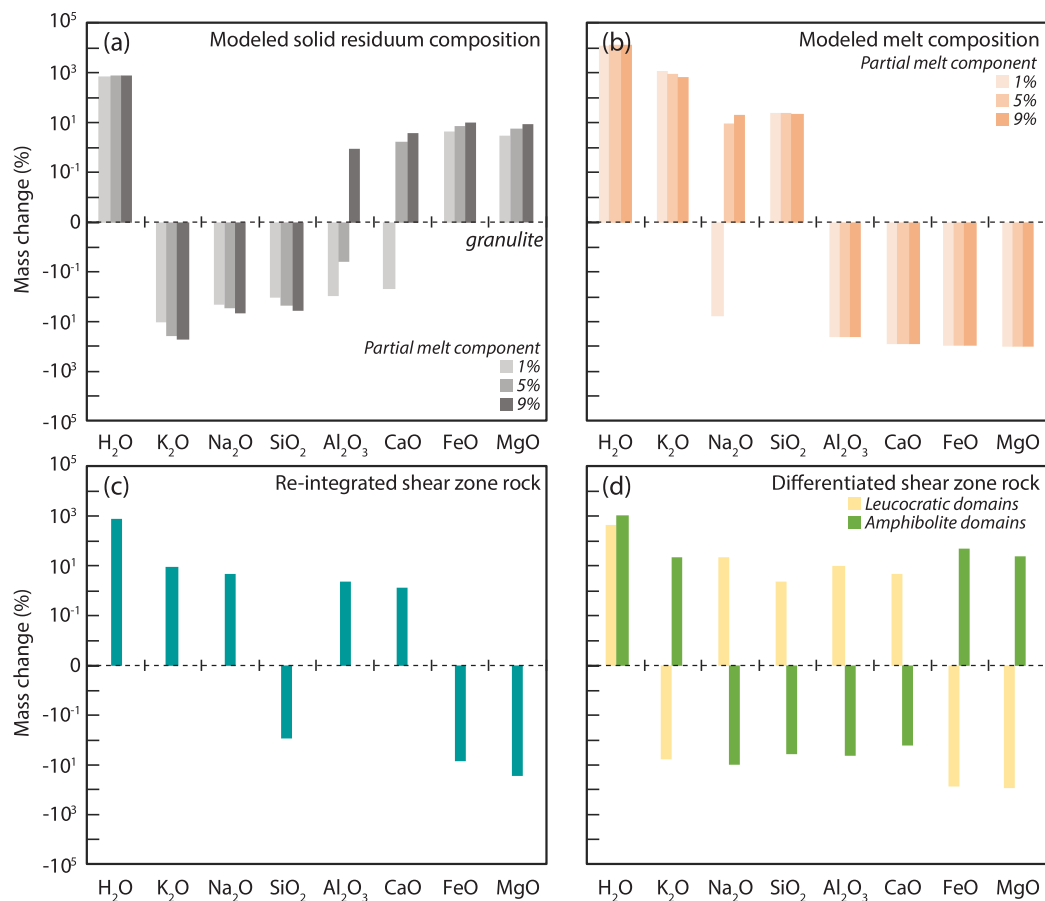


Figure 13

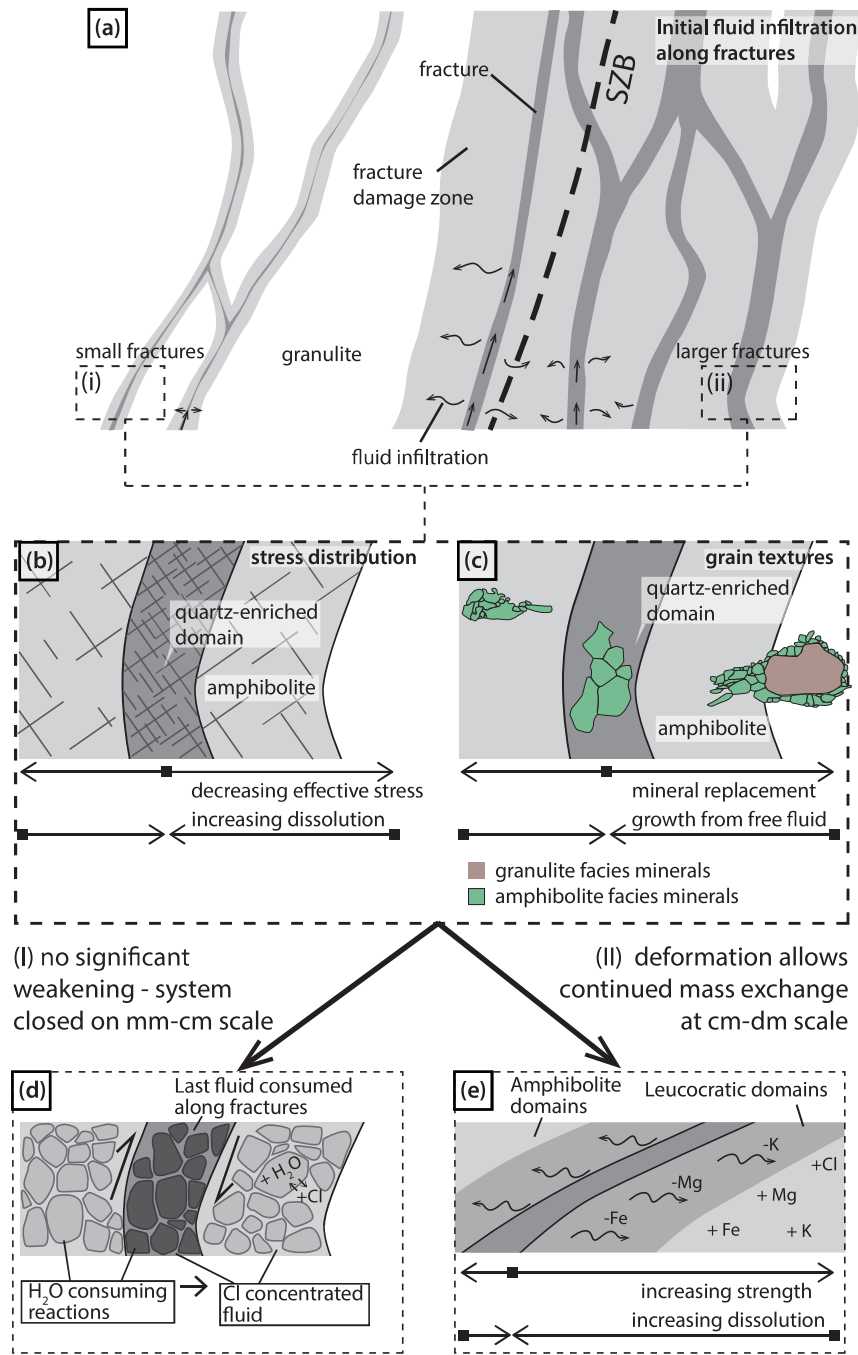


Table 1. Representative Whole rock analyses of major elements (XRF).

	Number of analyses (N)		2		3		1		1	
Density	2.87	2.86	2.83	2.89	2.80	2.80	2.89	2.80	2.80	2.80
Sample	Granulite	Amphibolite	Strained amphibolite	SE amphibolite	SE amphibolite	SE amphibolite	Shear zone amphibolite	Leucocratic domains	Re-integrated shear zone rock	Re-integrated shear zone rock
SiO ₂	50.1	49.4	50.1	0.18	0.020	0.21	48.3	51.3	49.7	49.7
Al ₂ O ₃	27.1	26.6	26.2	0.065	0.080	0.26	26.0	29.8	27.7	27.7
Fe ₂ O ₃	0.263	0.876	0.767	0.078	0.011	0.11	1.24	0.555	0.926	0.926
FeO	2.94	2.73	2.54	0.12	0.020	0.10	3.66	0.310	2.12	2.12
MnO	0.04	0.05	0.04				0.07	0.01	0.04	0.04
MgO	3.54	4.12	3.61	0.14	0.085	0.22	4.4	0.46	2.59	2.59
CaO	12.0	11.5	11.4	0.055	0.040	0.15	11.8	12.5	12.1	12.1
Na ₂ O	3.3	3.23	3.46	0.060	0.020	0.035	2.97	4.02	3.45	3.45
K ₂ O	0.262	0.231	0.425	0.0080	0.011	0.048	0.318	0.247	0.285	0.285
SO ₃	0.0255	0.0740	0.0847	0.0045	0.0060	0.022	0.0720	0.0710	0.0715	0.0715
CO ₃	0.150	0.300	0.250				0.200	0.100	0.150	0.150
Cl	0.0015	0.050	0.057	0.00071	0.018	0.014	0.095	0.0090	0.057	0.057
H ₂ O (LOI)	0.095	0.36	0.61	0.14	0.10	0.17	0.36	0.48	0.41	0.41
Total	99.8	99.5	99.5	99.4	99.6	99.9	99.6	99.9	99.6	99.6
Fe ^{tot}	3.53	3.91	3.59	5.31	3.28	3.28	5.31	3.28	3.28	3.28
H ₂ O (Thermocalc)	0.095	0.84	1.0	0.78	0.78	0.78	1.0	0.48	0.78	0.78